

RESEARCH ARTICLE | SEPTEMBER 03 2020

Effect of co-flow velocity ratio on evolution of poly-disperse particles in coaxial turbulent jets: A large-eddy simulation study

Anup V. Barve  ; Srikrishna Sahu  ; Kameswararao Anupindi  



Physics of Fluids 32, 093303 (2020)

<https://doi.org/10.1063/5.0017663>

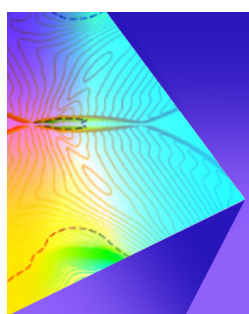


View
Online



Export
Citation

CrossMark



Physics of Fluids
Special Topic: Shock Waves

Submit Today!

Effect of co-flow velocity ratio on evolution of poly-disperse particles in coaxial turbulent jets: A large-eddy simulation study

Cite as: Phys. Fluids 32, 093303 (2020); doi: 10.1063/5.0017663

Submitted: 9 June 2020 • Accepted: 10 August 2020 •

Published Online: 3 September 2020



View Online



Export Citation



CrossMark

Anup V. Barve,  Srikrishna Sahu,  and Kameswararao Anupindi^a 

AFFILIATIONS

Department of Mechanical Engineering, Indian Institute of Technology Madras, Chennai 600036, India

^aAuthor to whom correspondence should be addressed: kanupindi@iitm.ac.in

ABSTRACT

In the present work, the particle-laden coaxial turbulent jet flow is studied using large-eddy simulation (LES). An Eulerian–Lagrangian framework is used to study the interaction between the continuous phase (air) and the discrete phase (glass bead particles). The solver is validated, using single-phase and particle-laden simulations, with reference data from experiments. A good match is observed between the present results and the reference data, for centerline velocity decay and radial profiles of axial velocity. Simulations are performed for three co-flow velocity ratios of 0, 1, and 1.5. The results pertaining to particle characteristics are presented for three different particle size-classes. The effect of the co-flow velocity ratio on the particle size–velocity correlation and velocity statistics of both phases are studied with an emphasis on understanding the differences in the particle dispersion due to co-flow around the central jet. It is observed that the particle size–velocity correlation is negative in the potential core region, and it becomes positive as one moves downstream. For heavy particles, the axial distance required to attain the same velocity as that of air increases with an increase in the co-flow velocity ratio. The size-conditioned particle number density profiles along the axial and radial directions of coaxial jets showed some interesting trends that could be explained based on the particle Stokes number effect. Significant radial dispersion of particles is realized when the corresponding Stokes number (St_L), defined based on large-scale turbulent eddies, is of the order of one. The axial evolution of the characteristic particle size exhibited non-monotonic trends for all co-flow ratios. Overall, the present work demonstrates potential application of LES for an in-depth study of dispersion of poly-disperse particles in turbulent coaxial jets.

Published under license by AIP Publishing. <https://doi.org/10.1063/5.0017663>

I. INTRODUCTION

Particle-laden turbulent flow can be regarded as a type of two-phase flow that consists of a continuous phase and a discrete phase. The continuous phase is also sometimes referred to as the carrier phase. These flows can be found in several engineering processes and applications such as pneumatic handling of solids, fluid catalytic cracking,¹ pulverized coal combustion,^{2,3} pure alumina production, internal combustion engines, liquid and solid propellant rocket motors, and gas-turbines. Particle-laden turbulent flows display rich and complex flow physics that motivates several researchers to understand the same.^{4,5} The behavior of the particles is quite distinct from that of the continuous phase owing to their inertia; as a result, particle-laden flows are more complex when compared to

single-phase flows. Due to the particular shape, size, and density of the particles, the response of them to turbulent flow varies. As a consequence, the particles may follow some turbulent eddies while being non-responsive to the other scales of the carrier phase turbulence.^{6,7} Therefore, the understanding of the mechanism of particle–turbulence interaction can be regarded as one of the main challenges in this type of flow.

Several researchers have carefully conducted experiments and analyzed single-phase and particle-laden coaxial jets. Champagne and Wignanski⁸ and Chigier and Beér⁹ investigated single-phase coaxial jets using experiments. They studied the effect of the co-flow velocity ratio on the length of the potential core, self-similar behavior of the jet in the downstream region, and the decay of the centerline velocity due to entrainment. Sadr and Klewicki,¹⁰ Tsuji

*et al.*¹¹ Hardalupas *et al.*¹² Sheen, Jou, and Lee,¹³ and Mostafa *et al.*¹⁴ have investigated particle-laden coaxial jet flows experimentally. They studied the effect of the co-flow velocity ratio on particle size and mass loading in a mono-disperse particle system. They found that the decay rate of the centerline velocity increases as particle-loading increases, and the particle dispersion is enhanced as the co-flow velocity ratio is increased. Fan, Zhao, and Cen¹⁵ experimentally investigated the aforementioned effects for poly-disperse particle systems. Their findings were similar to that of the mono-dispersed system. In addition, they observed that the particle concentration achieved a self-similar region in the zone where the coaxial jets have fully merged, and also, the lighter particles dispersed more when compared to the heavier particles.

Numerical simulation of particle-laden flows is an important tool for the design and development of multi-phase systems as it not only helps understand the flow physics but also interprets existing experimental data. Furthermore, numerical simulations could be easily extended to perform parametric studies for altered operating conditions.¹⁶ Often, an Eulerian-Lagrangian approach is used to model the carrier phase and the dispersed phase, respectively.¹⁷ Direct numerical simulations (DNSs),^{18–25} large-eddy simulations (LESs),^{26–31} and Reynolds-averaged Navier-Stokes (RANS)^{32–35} based simulations have all been used in the literature in order to study particle-laden flows. Typically in DNS, all spatial and temporal scales are resolved by the mesh used, and therefore, it is considered the most accurate numerical tool. DNS demands very fine meshes in order to resolve all the scales, which in turn requires huge computational resources. Therefore, DNS based investigations are used every so often. RANS based simulations can be put on the other side of the spectrum in terms of their computational resources. The computational resources required for performing RANS based simulations are orders of magnitude smaller in comparison with those required for DNS. However, RANS based simulations are not accurate for simulating particle-laden flows as was already established in the literature by Sommerfeld, Ando, and Wennerberg³⁶ and Apte *et al.*³⁷ In general, simulations that are based on LES can be put in between RANS simulation and DNS in terms of required computational resources. In LES, only the large energy containing eddies are resolved by the mesh and the effect of the small-scales on the large-scales is modeled using a sub-grid-scale (SGS) model. LES was shown to be superior to RANS simulation for the prediction of turbulence mixing and other physics.³⁸

As far as the numerical simulation of particle-laden flows in the coaxial configuration is concerned, there are a few studies available in the literature. Kannaiyan and Sadr³² and Aziz, Raiford, and Khan³⁹ performed RANS simulations on coaxial turbulent jets. Olson and Fuchs⁴⁰ and Askselvoll and Moin⁴¹ performed LESs on turbulent coaxial jets. Tkatchenko *et al.*⁴² performed both RANS simulation and LES for coaxial turbulent jets. Their study showed that LES models are superior to RANS simulation models in predicting the mean quantities. Abboud and Smith⁴³ performed LES on coaxial jets and examined the effects of using different synthetic inflow turbulence methods. Two synthetic inflow turbulence generation methods, namely, (i) the digital filter method (DFM) developed by Klein, Sadiki, and Janicka⁴⁴ and (ii) the synthetic eddy method (SEM) developed by Jarrin *et al.*,⁴⁵ were used in their study. The results obtained showed that both the DFM and the SEM are

effective in simulating coaxial turbulent jets. However, only a handful of works could be found that used LES for particle-laden coaxial jet flows. Apte *et al.*³⁷ performed LES of swirling coaxial particle-laden jets with a swirling flow introduced in the annular jet. Glass bead particles with size varying between 10 μm and 120 μm were introduced in the central jet, and their dispersion characteristics were studied. Recently, Pedel *et al.*²⁶ performed LES coupled with an Eulerian solver and studied the dispersion of poly-disperse particles. They used the Direct Quadrature Method of Moments (DQMOM) to track the particles in an Eulerian framework.

A review of the literature suggests that the effects of particle size, particle density, and solid loading (the ratio of mass flow rates of particles and the carrier phase) on particle dispersion are investigated only for mono-sized particle (mono-disperse suspension) systems. The characteristics of poly-disperse particles in turbulent coaxial jet flows have not been thoroughly investigated in the literature, yet. Several industrial applications, as discussed above, contain poly-disperse particles. The particles with a wide range of sizes with different inertia and relaxation time interact with a wide range of turbulent eddies with different length scales and timescales. In addition, in a gaseous jet, the turbulence is inhomogeneous and the turbulence spectrum evolves downstream of the nozzle exit. Apart from this, the co-flow around the central jet modifies the evolution of turbulence characteristics of the latter. Thus, the particle-turbulence interaction in coaxial jets presents a complex multi-scale two-phase flow, which is not yet fully understood and needs a systematic evaluation and characterization. In particular, the dispersion characteristics of poly-disperse particles require a detailed investigation due to its particle relevance. Therefore, the aim of the present work is to numerically study the above for three different co-flow velocity ratios using LES. The LES solver used in the present work is thoroughly validated for particle-unladen coaxial jets for all the co-flow ratios using reference experimental data found in the literature.⁵ The solver is also validated for a particle-laden single jet case using reference experimental data.⁵ Upon successful validation of the solver, the effects of the co-flow velocity ratio on the particle dispersion, downstream evolution of the particle Stokes number, particle size-velocity correlation, average velocity of the particles along the jet centerline, and downstream evolution of the average mean diameter (*AMD*) and Sauter mean diameter (*SMD*) are investigated and analyzed.

The remainder of this paper is organized as follows. The numerical formulation is presented in Sec. II that discusses the equations that govern the continuous and the discrete phases and the simulation setup including the geometry of the domain, the mesh, and the several boundary conditions used in the simulations. This is followed by Sec. III that contains the results of the grid sensitivity test, validation of the present solver, and the main contribution of the present work that is characterization and analysis of dispersion of poly-disperse particles in coaxial turbulent jets. Finally, Sec. IV summarizes the main findings of the present work and concludes this paper.

II. NUMERICAL FORMULATION

The governing equations for the continuous and the discrete phases are discussed in this section. All the simulations in the present

work are carried out using OpenFOAM 4.1.^{46,47} For the simulation of single-phase cases, the *pimpleFoam* solver is used, which is a transient solver for incompressible flows that uses the PIMPLE (merged PISO and SIMPLE) algorithm.^{46,47} For the simulation of multiphase flow cases, the multi-phase particle in cell solver known as *MPPICFoam* is used.

A. Continuous-phase modeling

The governing equations for the continuous phase are the filtered, incompressible continuity and Navier–Stokes equations and are given as follows:

$$\frac{\partial \bar{u}_i}{\partial x_i} = 0, \quad (1)$$

$$\frac{\partial \bar{u}_i}{\partial t} + \frac{\partial}{\partial x_j} (\bar{u}_i \bar{u}_j) = -\frac{1}{\rho} \frac{\partial \bar{p}}{\partial x_i} + \nu \frac{\partial^2 \bar{u}_i}{\partial x_j \partial x_j} - \frac{\partial \tau_{ij}^{SGS}}{\partial x_j} + S_i, \quad (2)$$

where \bar{u}_i indicates the filtered velocity vector, ρ is the density of the fluid, \bar{p} is the filtered pressure, ν is the kinematic viscosity of the fluid, and S_i is a source term that arises because of the presence of the particles. In Eq. (2), the term τ_{ij}^{SGS} is known as the residual stress tensor or sub-grid-scale (SGS) stress tensor. Closure of the filtered Navier–Stokes equations is achieved by modeling the residual stress tensor τ_{ij}^{SGS} . There are several SGS models that exist in the literature. The present study employs the dynamic k-equation SGS model developed by Kim and Menon.⁴⁸ In this model, an evolution equation for the SGS kinetic energy (k_{SGS}) is solved, and this is used as the velocity-scale in estimating the SGS viscosity. The evolution equation for k_{SGS} can be given as follows:

$$\frac{\partial k_{SGS}}{\partial t} + \bar{u}_j \frac{\partial k_{SGS}}{\partial x_j} = -\tau_{ij}^{SGS} \frac{\partial \bar{u}_i}{\partial x_j} - \varepsilon + \frac{\partial}{\partial x_j} \left(\nu_{SGS} \frac{\partial k_{SGS}}{\partial x_j} \right), \quad (3)$$

where on the right-hand side the first, second, and third terms denote the production, dissipation, and rate of transport of the SGS kinetic energy, respectively. The residual stress tensor τ_{ij}^{SGS} can be written as follows:

$$\tau_{ij}^{SGS} = \bar{u}_i \bar{u}_j - \bar{u}_i \bar{u}_j. \quad (4)$$

The SGS stress tensor, τ_{ij}^{SGS} , can be modeled in terms of SGS viscosity as follows:

$$\tau_{ij}^{SGS} = -2 \nu_{SGS} \bar{S}_{ij} + \frac{2}{3} \delta_{ij} k_{SGS}, \quad (5)$$

where the SGS kinematic viscosity ν_{SGS} is given by

$$\nu_{SGS} = C_k \Delta \sqrt{k_{SGS}}, \quad (6)$$

where Δ is the filter width, which is usually taken as the local grid size. Using simple scaling arguments, the dissipation rate is modeled as follows:

$$\varepsilon = C_\varepsilon k_{SGS}^{3/2} / \Delta. \quad (7)$$

The coefficient C_k occurring in Eq. (6) is given by

$$C_k = \frac{L_{ij} M_{ij}}{2 M_{ij} M_{ij}}, \quad (8)$$

where L_{ij} and M_{ij} arise because of the test filter and are given as follows:

$$L_{ij} = \widehat{\bar{u}_i} \widehat{\bar{u}_j} - \widehat{\bar{u}_i} \widehat{\bar{u}_j}, \quad (9)$$

$$M_{ij} = -\left(\Delta^2 \widehat{|\bar{S}| \bar{S}_{ij}} - \widehat{\Delta^2} |\widehat{\bar{S}}| \widehat{\bar{S}_{ij}} \right), \quad (10)$$

where \bar{S}_{ij} is the filtered strain rate tensor given by

$$\bar{S}_{ij} = \frac{1}{2} \left(\frac{\partial \bar{u}_i}{\partial x_j} + \frac{\partial \bar{u}_j}{\partial x_i} \right), \quad (11)$$

and the coefficient C_ε is obtained using the following expression:

$$C_\varepsilon = \frac{2\nu\widehat{\Delta} \left(\frac{\partial \widehat{\bar{u}_i}}{\partial x_j} \frac{\partial \widehat{\bar{u}_i}}{\partial x_j} - \frac{\partial \widehat{\bar{u}_i}}{\partial x_j} \frac{\partial \widehat{\bar{u}_i}}{\partial x_j} \right)}{\left(\widehat{\bar{u}_i} \widehat{\bar{u}_i} - \widehat{\bar{u}_i} \widehat{\bar{u}_i} \right)^{3/2}}, \quad (12)$$

where the hat symbol denotes quantities that are filtered on a test filter with a width of $\widehat{\Delta}$ that is usually taken to be 2Δ .

The volumetric particle–fluid interaction force, S_i , in the carrier phase momentum equation is calculated by averaging the forces acting on individual particles present in a computational cell, which is expressed as

$$S_i = -\frac{1}{dV} \left(\sum F_i^p \right). \quad (13)$$

It is worth discussing here the requirement of the particle induced source term in the SGS kinetic energy equation in the present simulations. Earlier, Wang and Squires³¹ in their work on a particle-laden turbulent channel incorporated the sub-grid velocity in the calculation of the particle forces. However, they noticed negligible effect of this sub-grid velocity. They noted that the relative difference between the SGS velocities and the resolved fluctuation velocities is greatest near the wall, and it reduces as one moves away from the wall. However, incorporation of the SGS velocities in the particle drag calculations yielded no effect. Therefore, they concluded that no additional source term in the k_{SGS} equation could be considered. Tabib and Schwarz⁴⁹ introduced a production term in the SGS transport equation to handle the bubble induced turbulence. This is done primarily to account for the higher volume fraction of the bubbles in the wakes. The bubble induced turbulence is modeled as the energy input coming from the forces acting between the gas bubbles and the surrounding liquid and the local slip velocity. The motivation to include the source term in the k_{SGS} equation stems from high volume fraction as well as the presence of bubbles, which may break-up into smaller segments as they travel downstream. Bharadwaj, Rutland, and Chang⁵⁰ and Bharadwaj and Rutland⁵¹ proposed a source term at the subgrid-scale level in the k_{SGS} equation in their LES of liquid spray atomization. The required sub-grid fluctuations were calculated using an approximate deconvolution method (ADM). These SGS fluctuations are further used only in the source term (W_{SGS}) in the k_{SGS} equation, but these were not used to correct the gas phase velocity in the Lagrangian calculations. The incorporation of the W_{SGS} term corresponds to the work done by the gas on the gas–liquid interface, and its inclusion improved the penetration length of the spray. The above simulations were mainly for an evaporating liquid spray in which the droplets as they emanate from the nozzle evaporate as they percolate into the domain. In addition, near the nozzle, the droplets further break-up to smaller sizes. In such a case, the source term, W_{SGS} , is considered to be important as it enables correct prediction of the spray evolution into the domain. However, even for spray applications, non-zero values of W_{SGS} were obtained only in the near nozzle exit spray region.

Further downstream of the spray injection, the values of W_{SGS} can be noted to be zero. This indicates that the additional source term in the k_{SGS} equation is only important in the near nozzle exit region for liquid spray applications.

The above discussion suggests that the use of a source term in the k_{SGS} equation is required (i) when the particle mass loading is high, for instance, in liquid sprays (ii) where the droplets are evaporating and becoming smaller as they percolate into the domain and (iii) only in the near nozzle exit region where the source term plays some role. In the present work, as rigid particles are used, which do not breakup and/or evaporate, their mass loading is low. Owing to the aforementioned reasons, the authors believe that the absence of a source term in the k_{SGS} equation in the present work does not affect the behavior of the particles. Hence, a source term is not included in the k_{SGS} equation in the present study similar to some of the other works in the literature.^{31,52,53} Moreover, as will be shown later in Sec. III B, very good agreement between the present simulation and experiments is obtained for the particle-laden jet, which supports the above assumption.

B. Discrete-phase modeling

The discrete phase is modeled using Newton's second law of motion given as follows:

$$\frac{dx_i^p}{dt} = u_i^p, \quad (14)$$

$$m_p \frac{du_i^p}{dt} = \sum F_i^p, \quad (15)$$

where x_i^p and u_i^p denote the position vector and the velocity vector of an individual particle, respectively, and F_i^p denotes summation of all the force vectors acting on the particle. Next, the different forces acting on the particles are discussed. The drag force is the most important force acting on the particle and is expressed as

$$F_i^D = C_d \frac{\pi d_p^2}{8} (\bar{u}_i - u_i^p) | \bar{u}_i - u_i^p |, \quad (16)$$

where d_p is the diameter of the particle, \bar{u}_i is the local, instantaneous, filtered velocity vector of the fluid, u_i^p is the instantaneous velocity vector of the particle, and C_d is the drag coefficient for the particle. The value of C_d is found using correlations of Putnam,⁵⁴ as given by

$$C_d = \begin{cases} \frac{24}{Re_p} (1 + \frac{1}{6} Re_p^{2/3}), & \text{for } Re_p \leq 1000 \\ 0.424, & \text{for } Re_p > 1000, \end{cases}$$

where Re_p is the particle Reynolds number given by $Re_p = \frac{d_p |\bar{u}_i - u_i^p|}{\nu}$. The other force that is considered on the particles, in the present work, is the gravitation force. It is expressed as follows:

$$F_i^g = m_p g_i \left(1 - \frac{\rho}{\rho_p} \right), \quad (17)$$

where ρ and ρ_p are the density of the fluid and the particle, respectively, and g_i is the acceleration due to gravity vector taken as $(0, -9.81, 0)$ m/s². In the present simulations, the density of the particles is much higher (nearly 800 times) than that of the fluid. Thus, both the virtual mass effect and the Basset history terms can

be safely neglected in the particle equation of motion as reported by Wang and Squires,³¹ Toschi and Bodenschatz,⁵⁵ and Olivieri *et al.*⁵⁶ Because of the same reason, the pressure gradient term can also be neglected as reported by Crowe *et al.*⁵⁷ In addition, this is further justified as the characteristic particle size is similar to the Kolmogorov length scale of turbulence. Thus, the velocity gradient across a particle can be ignored.

The size distribution of the particles at the inlet to the domain is specified using Rosin–Rammler particle distribution.^{57–59} According to this distribution, the mass fraction, ψ , of particles with a diameter greater than d_p is given by $\psi = e^{-(d_p/d_0)^n}$, where n is the size distribution parameter that controls the spread of the distribution, d_p is the particle diameter, and d_0 represents the mean particle size.

C. Simulation setup

A three-dimensional cylindrical geometry is used as the solution domain, as shown in Fig. 1. The domain extends $40R$ in the axial direction and $40R$ in the radial direction, where R is the radius of the central jet. With reference to this figure, the boundary indicated by IB_1 is used as the inflow boundary for the central jet. A fully developed turbulent velocity profile for the pipe flow is used as the velocity boundary condition for the central jet inflow boundary, IB_1 , given as follows:

$$\frac{\bar{u}}{u_e} = \left(1 - \frac{r}{R} \right)^{\frac{1}{7}}, \quad (18)$$

where \bar{u} is the filtered x -component of velocity and u_e is the maximum x -component of velocity at the nozzle exit of the central jet, which is taken as 11.7 m/s that is the same as in reference experiments.⁵ The diameters of the central jet and annular jet are taken to be the same as used in reference experiments.⁵ The diameter of the central jet is $2R = 14.224$ mm, and the inner and outer diameters of the annular jet (co-flow jet) are $D_i = 15.875$ mm and $D_o = 31.852$ mm, respectively. A fully developed turbulent velocity profile, obtained from reference experiments,⁵ is used on the annular jet inflow boundary, IB_2 . The ratio between the maximum velocity of the annular jet and the maximum velocity of the central jet is defined as the velocity ratio denoted α . In the present work, $\alpha = 0$, 1, and 1.5 are investigated. In the case of $\alpha = 0$, referred to herein as a single jet, the central jet alone issues the fluid into the domain and there is no annular jet flow. A no-slip boundary condition for

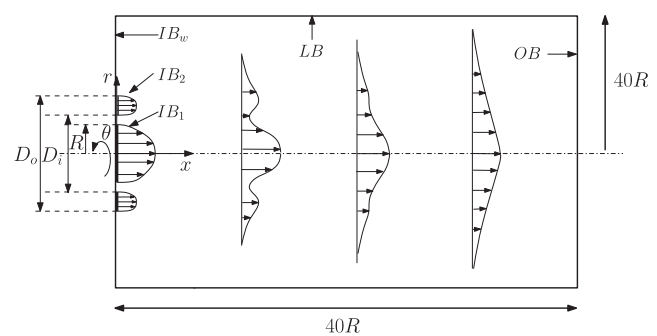


FIG. 1. Schematic of the simulation domain (not to scale) depicting several boundaries and downstream evolution of the axial component velocity.

velocity is used on the boundary, IB_w . A radial entrainment velocity with a magnitude of 4% of u_e is specified on the later boundary denoted LB . The radial entrainment velocity on the lateral boundary (LB) was provided in order to aid the entrainment of the fluid into the domain without forming a large-scale recirculation region. This is done as per the recommendations provided in the article by Dejoan and Leschziner.⁶⁰ They used this boundary condition for simulating a wall jet and suggested that the dynamics of the flow would not change because of this. In the present work, the validation studies presented later (in Fig. 5) for the case of a single jet show a good match with the experimental results. This indicates that the dynamics of the jet do not change due to the lateral boundary velocity condition. A convective outflow boundary condition proposed by Orlanski⁶¹ is applied on the outflow boundary of the domain denoted OB . On this boundary, OB , a uniform value for pressure is prescribed. On all other boundaries, a homogeneous von Neumann boundary condition is used for pressure. The Reynolds number of the flow, based on the maximum velocity at the central jet nozzle exit, u_e , and the inlet diameter of the central jet, $2R$, is taken as 8400, which is the same as that in the reference experiments.⁵ In the present work, the spatial derivatives are discretized using the second-order accurate scheme and the temporal terms are discretized using the second-order accurate implicit time-stepping scheme.

Eddy-resolving methods such as LES require specification of instantaneous (sum of the time-averaged and fluctuation) values

of variables on all inflow boundaries. As discussed earlier, the time-averaged values of velocity on the inflow boundary, IB_1 , are obtained using Eq. (18) and those on the inflow boundary, IB_2 , are obtained from the reference experiments. The specification of velocity fluctuations is an active area of research and can be accomplished using several methods as described in the review articles.^{62–64} In the present work, owing to the simplicity of the method, the random fluctuation generation method is used. In this method, time dependent random data are superimposed on the time-averaged velocity profile in order to obtain an instantaneous velocity field on the inflow boundaries IB_1 and IB_2 . An existing *turbulentInlet* functionality in OpenFOAM⁴⁶ is used that generates the instantaneous velocity field as follows:

$$u_i^{n+1} = \beta u_i^n + (1 - \beta)(1 + s C_{rms}) \langle \bar{u}_i \rangle, \quad (19)$$

where u_i^{n+1} is the instantaneous velocity field at the next time-step level, $\langle \bar{u}_i \rangle$ is the time-averaged filtered velocity field, n and $n + 1$ indicate the present and the next time-step index, respectively, β specifies the fraction of the previous time-step value to be used, C_{rms} is the root-mean-square (rms) coefficient, and s is the scale of fluctuation. In the present simulations, values of $\beta = 0.1$ and $s = 0.02$ are used. Throughout this manuscript, angle brackets, $\langle \cdot \rangle$, are used to represent time-averaged values.

The computational domain together with the mesh used in the present study is shown in Fig. 2. The cells are refined near

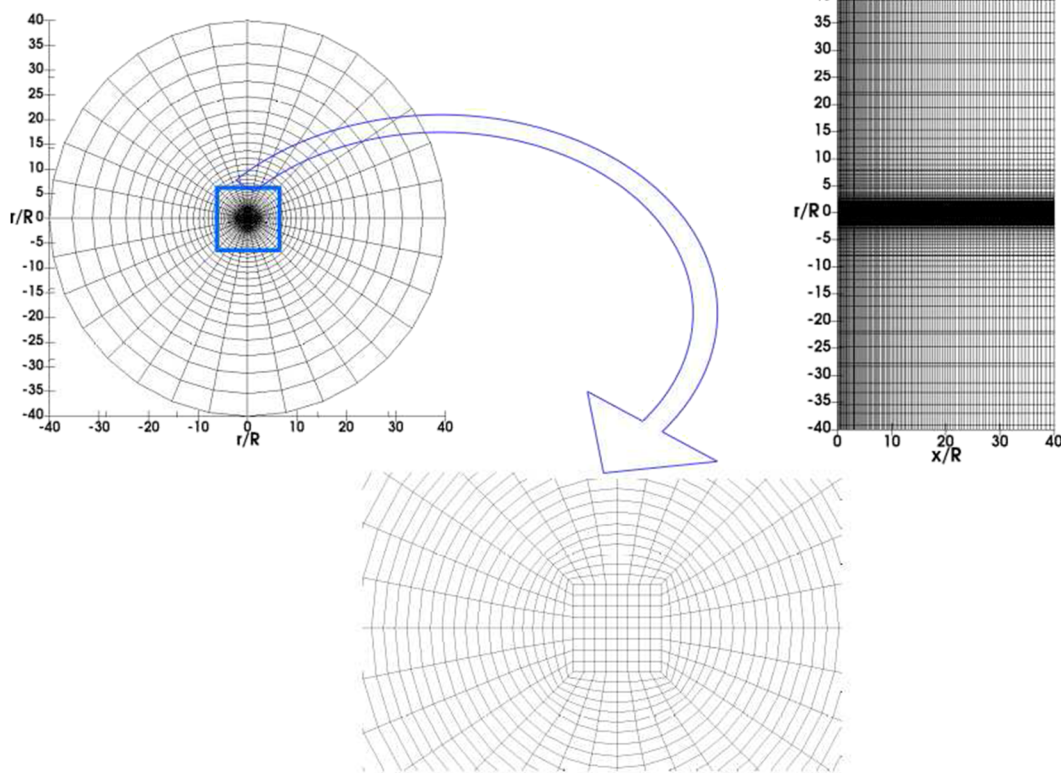


FIG. 2. Two views of the mesh used in the present simulations. A zoom-in view of the central portion of the domain in the radial-circumferential plane is also shown.

the central-core and the annular jet regions, and the grid spacing increases as one moves away from the central jet region. As can be seen from this figure, the central jet region consists of a square mesh that avoids the point of singularity that is otherwise observed in axisymmetric structured grids. This further enables the particle-search algorithms to work efficiently as discussed by Apte *et al.*³⁷ Furthermore, the grid spacing also increases as one moves away from the inlet boundaries along the axial direction.

Budilarto⁵ in his experiments used glass bead particles with a density of 2500 kg/m^3 . In the present simulations, particles with the same density are injected in the central jet, however, at zero initial velocity. In the reference experiments,⁵ the particles were injected laterally into a long pipe much ahead of the nozzle exit. Thus, at the nozzle exit, the velocity of particles varies according to the gas velocity profile, and in addition, the particle–gas slip velocity is not zero and specified only at the center. Hence, owing to the limitations in specifying particle velocity across the nozzle exit, the initial velocity of all particles was specified as zero. The mass loading of the particles is 0.09% of the inlet mass flux of the continuous phase. The particle diameter specification at the inlet of the domain follows Rosin–Rammler distribution^{57–59} with minimum, mean, and maximum diameters of $10 \mu\text{m}$, $50 \mu\text{m}$, and $100 \mu\text{m}$.

III. RESULTS

In this section, the results obtained using the present solver are discussed. First, a grid sensitivity test is performed to establish consistency of the solver used. Thereafter, the solver is validated for coaxial jets without particles for different velocity ratios, $\alpha = 0, 1$, and 1.5 . Coaxial jets with particles are also validated by comparing the present results with the reference experimental data⁵ from the literature. Upon successful validation of the solver, the main results are presented that include evolution of the particle Stokes number in the jet, particle size–velocity correlation, mean velocity of particles, and, finally, the dispersion of the poly-dispersed particles. For each of the above results, the interest, in particular, is on the influence of the co-flow velocity ratio. The particle characteristics are discussed for three different size-classes, viz., $25 \mu\text{m}$ – $50 \mu\text{m}$, $50 \mu\text{m}$ – $75 \mu\text{m}$, and $75 \mu\text{m}$ – $100 \mu\text{m}$. The width of the size-class was selected as a trade-off between poor statistics (when the width

is too small) and size-averaged statistics (when the width is too large).

A. Grid sensitivity test

To establish consistency of the present solver, a grid sensitivity test is performed. Three different grid resolutions consisting of 1.2 , 1.8 , and 2.1×10^6 cells are tested. All the three cases are simulated for a velocity ratio of $\alpha = 1$. Figure 3 shows the radial profiles of the axial component of velocity, normalized using the maximum velocity at the nozzle exit u_e , at indicated axial locations for the three mesh resolutions considered. The reference data from experiments are also shown⁵ for direct comparison. Overall, a good match can be noted between the present results and the reference experimental data.⁵ Only a marginal improvement was obtained for the cases consisting of 1.8×10^6 and 2.1×10^6 cells when compared with the case consisting of 1.2×10^6 cells. From the grid sensitivity test, the mesh consisting of 1.8×10^6 cells is chosen for performing all further simulations.

B. Validation

1. Single jet case, $\alpha = 0$, without particles

First, the case without any co-flow is studied. The axial variation of the centerline axial velocity is shown in Fig. 4 for a co-flow ratio of $\alpha = 0$. The centerline velocity decay follows the typical profile for a single round jet. The evolution of the axial centerline velocity can be demarcated into two regions. The first region, where the centerline velocity remains constant, is known as the potential core region, and the length of this region is noted to be approximately $10r$. In the second region, downstream of the potential core, the jet begins to spread by entraining the surrounding fluid, and as a result, the centerline velocity decays quickly.

The radial profiles of the axial component of velocity are shown in Fig. 5 for the indicated axial locations. It can be noted that a self-preserving velocity profile is observed beyond $x/R = 20$. A good match can be seen between the present results and the experimental data. As one moves from the location $x/R = 2$ to $x/R = 30$, a gradual spread of the jet in the r -direction and a corresponding decrease in the centerline axial velocity can be noted. Having compared the

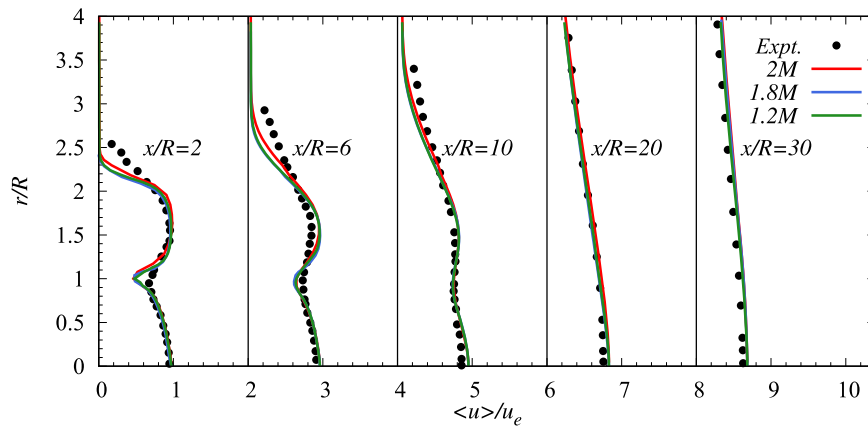


FIG. 3. Radial profiles of $\langle u \rangle / u_e$ at indicated axial locations for a velocity ratio of $\alpha = 1$.

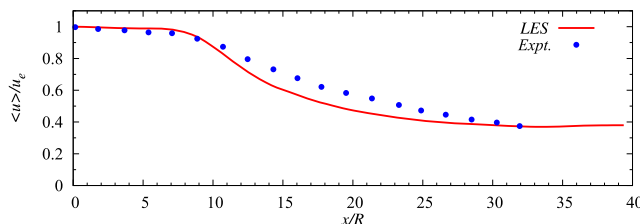


FIG. 4. Axial variation of the centerline axial velocity for the co-flow ratio $\alpha = 0$.

centerline velocity decay and the radial profiles of the time-averaged axial velocity, next we turn to a comparison of the second-order statistics obtained from the present LES results and the reference experimental data. Frames (a)–(d) of Fig. 6 depict the radial profiles of the axial-component of the normalized velocity fluctuation, u_{rms}/u_e , at $x/R = 6$ through $x/R = 30$. It can be noted that the results obtained using the present solver are able to predict the radial variation of velocity fluctuations both qualitatively and quantitatively with respect to the reference data.⁵ Similar to the axial evolution of the time-averaged axial velocity, the u_{rms}/u_e profiles also spread in the r -direction and the peak values of these profiles reduce as one moves downstream. Peak values in the profiles of u_{rms}/u_e could be

noted at $x/R = 6$ and $x/R = 10$, whereas further downstream, owing to the spreading of the jet, no such peaks could be noticed at locations $x/R = 20$ and $x/R = 30$.

2. Coaxial jet case, $\alpha = 1$, without particles

Next, as part of the validation study, we consider the coaxial jet case with a velocity ratio $\alpha = 1$ without involving particles. Figure 7 presents the evolution of $\langle u \rangle / u_e$ for the coaxial jet case with $\alpha = 1$ without particles obtained from the present results together with the reference experimental data.⁵ Unlike the single jet case, here, it can be noted that there is a sudden decrease in $\langle u \rangle / u_e$ near the nozzle exit. Budilarto⁵ reasoned out that such a behavior is because of the annular jet drawing fluid from the central jet in order to fulfill the entrainment requirements. Following this initial dip in $\langle u \rangle / u_e$, however, the axial velocity remains constant further up to about 12 r after which the velocity begins to decay similar to the single jet case. Therefore, similar to the single jet case, the axial evolution of $\langle u \rangle / u_e$ is characterized by two distinct regions: the potential core region and then the decay region. In the coaxial jet case with $\alpha = 1$, the potential core is noted to be longer and the decay rate of the centerline axial velocity is noted to be smaller in comparison with those in the single jet case. It can be noted that the potential core region, although clearly visible for the present experiments, is small in the

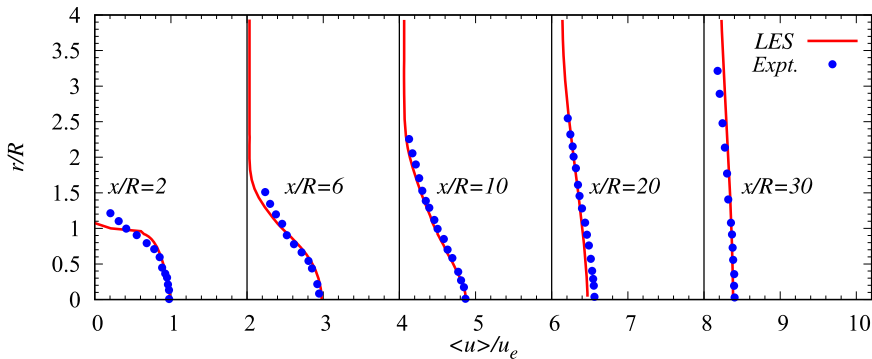


FIG. 5. Radial profiles of the axial component of velocity at indicated axial locations for the single jet case $\alpha = 0$.

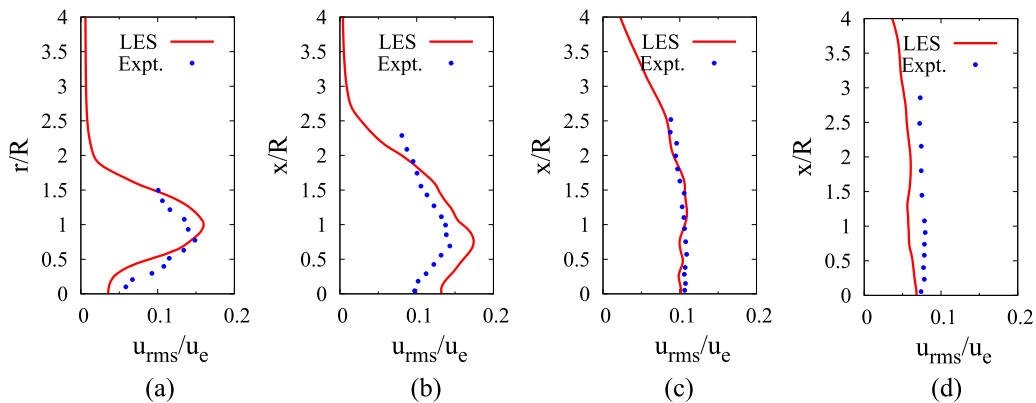


FIG. 6. Radial profiles of the normalized axial component of the velocity fluctuation, u_{rms}/u_e , for the single jet case with $\alpha = 0$ at locations (a) $x/R = 6$, (b) $x/R = 10$, (c) $x/R = 20$, and (d) $x/R = 30$.

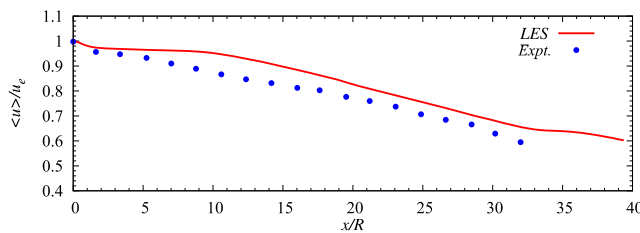


FIG. 7. Axial evolution of the centerline axial velocity for a co-flow ratio $\alpha = 1$.

reference experiments. Overall, the qualitative trend of centerline velocity decay is captured by the present results in comparison with the reference data.

Next, we turn to a comparison of the radial profiles of $\langle u \rangle / u_e$ at different axial locations. Figure 8 shows the radial profiles of $\langle u \rangle / u_e$ at indicated axial locations for the present experiments and for the reference experiments for a co-flow velocity ratio of $\alpha = 1$. From this figure, it can be noted that similar to the single jet case, the centerline value of $\langle u \rangle / u_e$ decreases and the jet spreads in the radial direction as one moves in the downstream direction. At $x/R = 2$, three distinct profiles ($0 < r/R < 1$; $1 < r/R < 2.5$; and $r > 2.5$) can be noticed, which eventually merge together into a smooth profile by $x/R = 20$ and beyond. This represents the interaction and merging of the central and the annular jets eventually into a single continuous jet. As the two jets exit the nozzle, they quickly interact and form shear layers. From this figure, it can also be seen that the peak value of the annular jet velocity tends to decrease at a higher rate in comparison with that of the central jet. The profiles obtained at $x/R = 20$ and $x/R = 30$ show that the radial profiles of $\langle u \rangle / u_e$ for $\alpha = 1.0$ are similar to those for $\alpha = 0$, except that the magnitude of velocity for the $\alpha = 1$ case is higher. This implies that for the case of $\alpha = 1$ by $x/R = 20$, the two jets have merged completely to form a single jet.

3. Coaxial jet case, $\alpha = 1.5$, without particles

Next, we consider another coaxial jet case with a co-flow velocity ratio of $\alpha = 1.5$. In this case, as the value of $\alpha > 1$, the time-averaged velocity of the annular jet is larger than that of the central jet. Figure 9 depicts the axial evolution of $\langle u \rangle / u_e$ for the present

results and for the reference experimental data.⁵ From this figure, three distinct regions could be identified for the evolution of $\langle u \rangle / u_e$. The first region that corresponds to $0 < x/R < 8$ can be noted as the potential core region. In this region, a sudden reduction in $\langle u \rangle / u_e$ could be noticed in the immediate exit from the nozzle for both simulations and experiments. This sudden decrease is because of the entrainment of the fluid from the central jet region to the annular jet region (which is at a higher velocity). The second region could be identified in the range of $10 < x/R < 15$. In this region, the inner shear layer from the annular jet approaches the centerline of the central jet. This is because of the relatively faster fluid from the annular jet mixing with the fluid in the central jet, thereby increasing the magnitude of $\langle u \rangle / u_e$. For this enhanced mixing, the second region could be called a mixing region of the coaxial jet flow. Finally, a third region could be identified as the region beyond $x/R > 15$. In this region, the annular and the central jets merge to form a single jet. The magnitude of the axial velocity begins to decay in this region as one moves further downstream along the direction of the jet. In comparison with the coaxial jet case with $\alpha = 1$, the decay rate of $\langle u \rangle / u_e$ is smaller in the present case. For example, at $x/R = 30$, $\langle u \rangle / u_e \approx 0.9$ for the coaxial jet case with $\alpha = 1.5$, whereas $\langle u \rangle / u_e \approx 0.7$ for the case with $\alpha = 1$; this is of course a consequence of the higher momentum fluid that is injected through the annular jet in the former case.

Next, we present the radial profiles of $\langle u \rangle / u_e$. Figure 10 depicts the radial profiles of $\langle u \rangle / u_e$ at several axial locations along the axis of the jet for a co-flow velocity ratio of $\alpha = 1.5$. Similar to the $\alpha = 1$ case, three distinct profiles can be noticed at $x/R = 2$, which merge further downstream to form a smooth continuous profile by $x/R = 20$. Some deviation between the present results and the reference data could be observed near the nozzle exit as depicted by the profile at $x/R = 2$; however, as one moves downstream from $x/R = 6$ and beyond, a better match could be observed.

To appreciate the complexity of the simulation, instantaneous vortical structures are educed next. A qualitative picture of the unsteady turbulent jet flow could be obtained by looking at the iso-surface of Q-criterion. Figure 11 depicts a qualitative picture of the evolution of vortical structures for the single and the coaxial jet cases without involving particles. Frames (a) and (b) of this figure depict the iso-surface of Q-criterion for $\alpha = 0$ and $\alpha = 1.5$, respectively. For the single jet case, small vortical structures could be observed

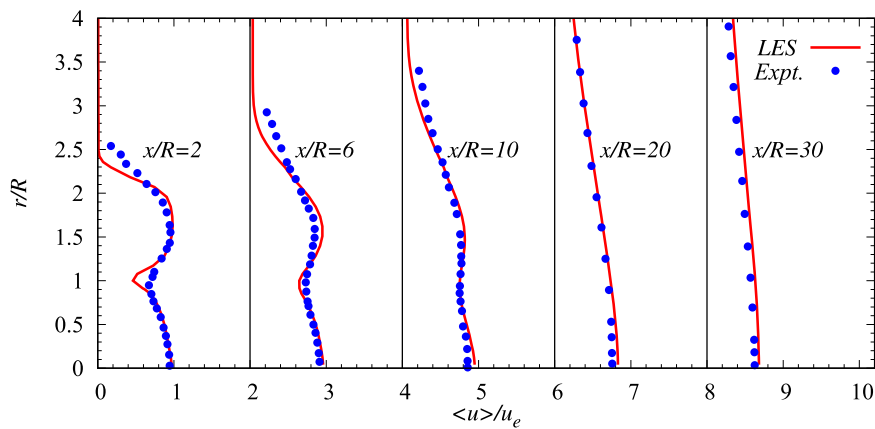


FIG. 8. Radial profiles of the axial component of velocity at indicated axial locations for a co-flow ratio of $\alpha = 1$.

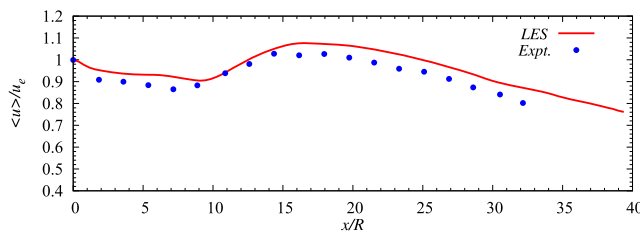


FIG. 9. Axial evolution of the centerline axial velocity for a co-flow velocity ratio of $\alpha = 1.5$.

right from the inlet to the domain. Further downstream, these vortical structures can be seen to strongly interact with each other and grow, which qualitatively depicts the edge of the shear-layer. For the co-flow case with $\alpha = 1.5$, the vortical structures at the inlet to the domain span a wider region owing to the co-flow. This wider extent of the vortical structures can be seen at all downstream locations for the co-flow case in comparison with the single jet case for the same value of Q-criterion. Beyond $x/R = 12$, it can be noted that the vortical structures look similar between the two cases considered here.

4. Single jet case, $\alpha = 0$, with particles

Having validated the present solver for the single and coaxial jets cases without involving particles, in this section, we turn to the validation by considering the presence of the particles. Particles with a uniform diameter of $d_p = 70 \mu\text{m}$ are injected through, IB_1 , the inlet to the central jet, similar to the reference experiments.⁵

Figure 12 depicts the centerline velocity decay of the continuous phase laden with particles for the present simulations and for the reference experiments. The corresponding profiles of the single jet case, $\alpha = 0$, without particles are also shown for the sake of comparison. It can be noted that for both the present simulations and for the experiments, beyond $x/R = 15$, the centerline velocity of the gas phase is smaller for the case laden with particles in comparison with the case that does not involve particles. We note the modification of the gas velocity, though small, may not be

anticipated considering very low particle to gas mass loading that ensures one way coupling (no influence of particles on gas momentum). This is possibly due to acceleration of the particles beyond the gas velocity such that a part of the momentum of the gas phase is now extracted by the particles. Next, notice that the computational results are in excellent agreement with the experimental results for gas velocity within the potential core of the jet; however, in a fully developed zone, some underestimation by the simulations is evident. This is true for co-flow ratios $\alpha = 1$ and $\alpha = 1.5$ as well, as presented earlier. The deviation of the present results when compared to the reference experimental data is attributed to the fact that the particles are injected at zero initial velocity in the simulations, whereas they are injected at the same speed as the gas phase in the experiments. These particles that are injected at zero velocity at the inlet to the domain would absorb more momentum from the gas phase to accelerate, thereby reducing the momentum of the gas phase. In the experiments, however, as the particles are already at the speed of the gas phase, they will not decelerate the flow of the gas much.

Now that the solver is thoroughly validated for coaxial jets with and without particles, we turn to a qualitative description of the jet flow laden with particles. Frames (a)–(c) of Fig. 13 depict the out-of-plane contours of instantaneous vorticity magnitude of the gas phase together with the instantaneous location of some representative particles for $\alpha = 0, 1$, and 1.5 , respectively. For all the cases, the particles are injected only through the central jet. From frames (b) and (c), it can be noted that the shear layers that emanate from the central jet and annular jet start to interact by $x/R \approx 8$ for $\alpha = 1$ and 1.5 cases. For the case of $\alpha = 0$, the injected particles can be found to be within $-1 < r/R < 1$ only until $x/R \approx 10$, beyond which they start to disperse radially because of the turbulent gas phase that is now wide-spread in the radial direction. However, for the coaxial jet cases with $\alpha = 1$ and 1.5 , the injected particles can be found to be closer to the jet axis, $-1 < r/R < 1$, almost until $x/R \approx 16$, beyond which they start to disperse radially similar to the single jet case. Therefore, it can be reasoned out that the annular jet contains the particles, which are injected through the central jet, near the jet axis until farther downstream. Beyond $x/R = 24$, it can be observed that both the gas phase and the particles have dispersed to larger radii for all co-flow velocity ratios of 0, 1, and 1.5. These plots set the stage for the main findings

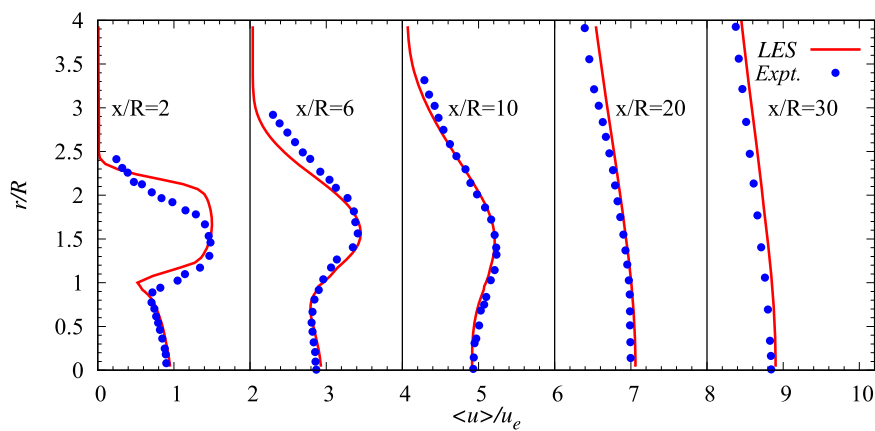


FIG. 10. Radial profiles of the axial component of velocity at indicated axial locations for a co-flow velocity ratio of $\alpha = 1.5$.

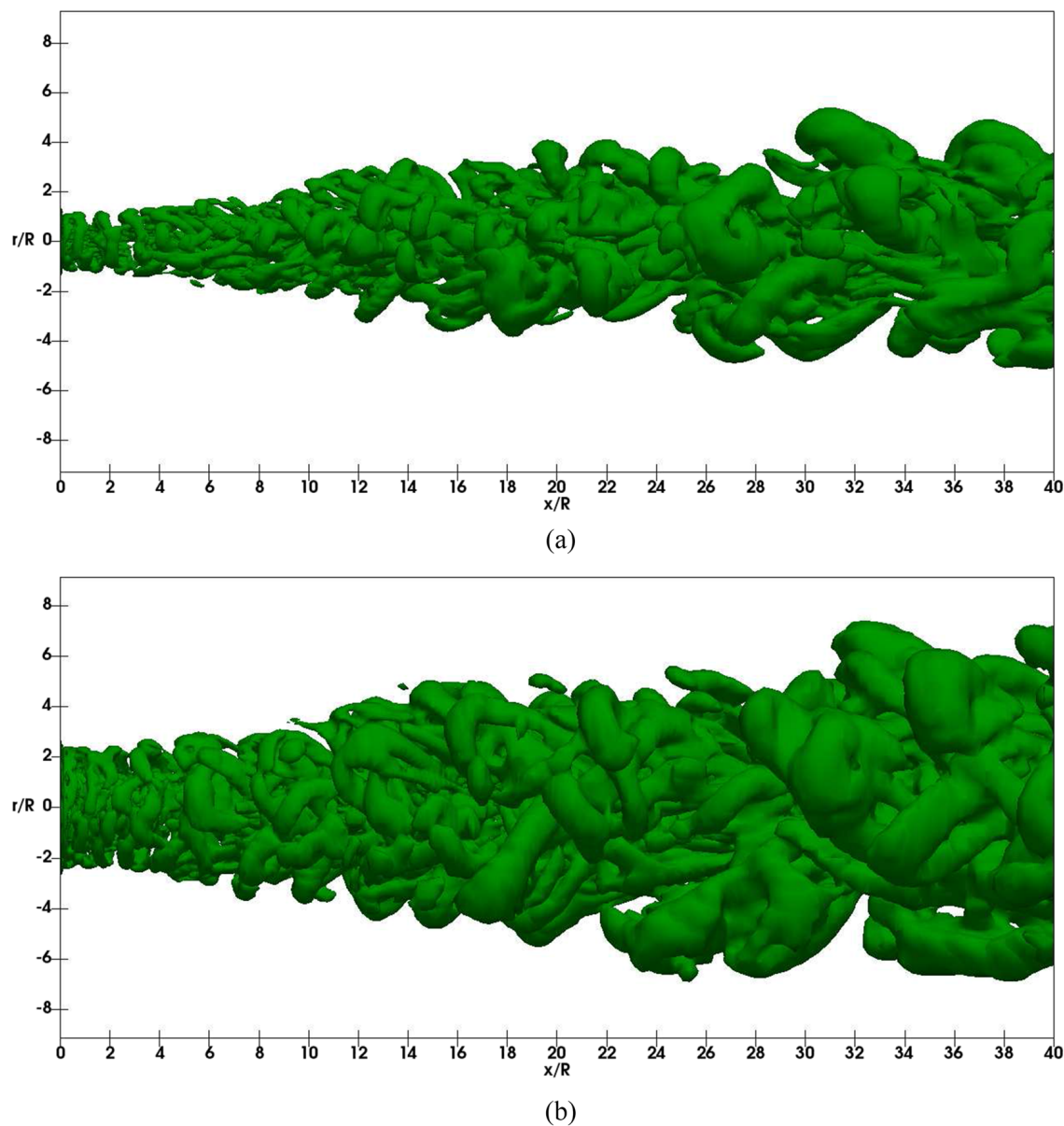


FIG. 11. Iso-surface of Q-criterion for co-flow ratios (a) $\alpha = 0$ and (b) $\alpha = 1.5$.

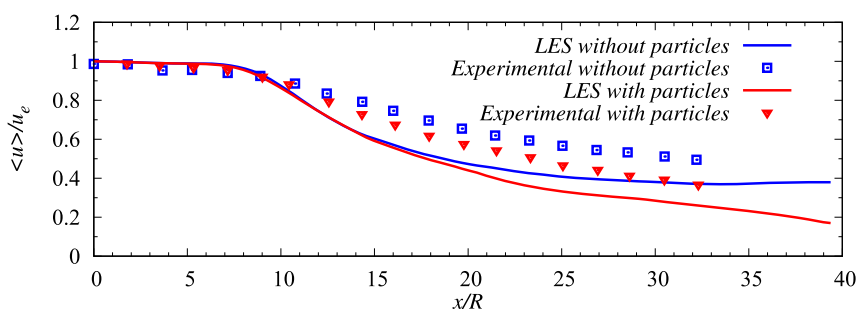


FIG. 12. Centerline velocity decay with mono-dispersed particles of $70 \mu\text{m}$ diameter for $\alpha = 0$.

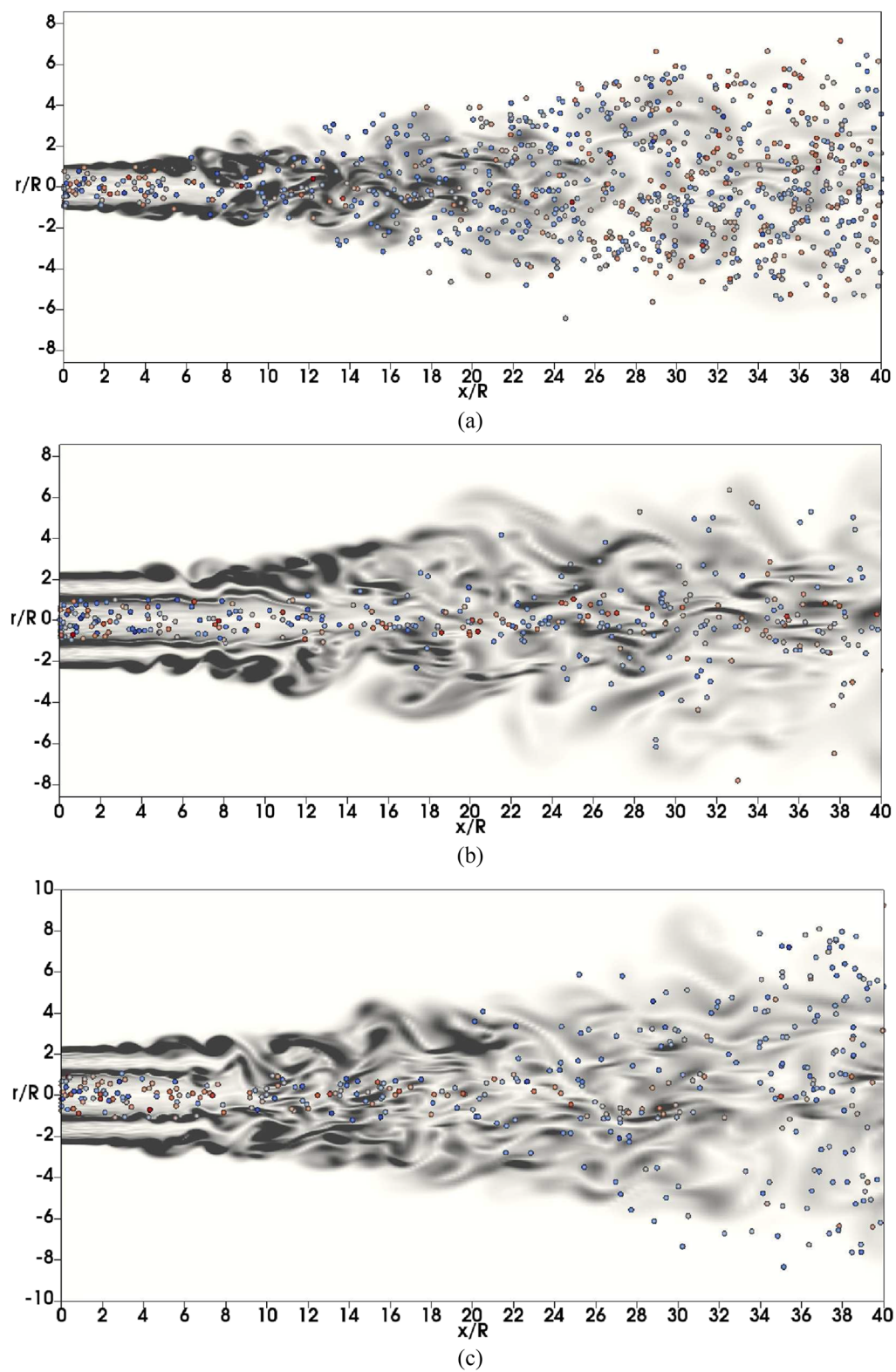


FIG. 13. Instantaneous contours of the out-of-plane vorticity magnitude together with instantaneous particle positions for co-flow ratios (a) $\alpha = 0$, (b) $\alpha = 1$, and (c) $\alpha = 1.5$.

of the present work using particle-laden coaxial jets, and the same is discussed in what follows.

C. Particle Stokes number and its evolution in the particle-laden jet

The calculation of the particle Stokes number is important to study the dispersion of particles injected in turbulent jets. For this reason, the particle response time is calculated that characterizes the capability of the particles to react to sudden changes in velocity of the carrier phase flow (gas flow). Assuming that the particle Reynolds number is less than one, $Re_p < 1$, and the drag coefficient is inversely proportional to the Reynolds number, the particle response time, τ_p , can be expressed as

$$\tau_p = \frac{\rho_p d_p^2}{18\mu_f}, \quad (20)$$

where ρ_p is the density of the particle, d_p is the diameter of the particle, and μ_f is the dynamic viscosity of the gas. The particle Stokes number, St , then can be defined as the ratio of the particle response time, τ_p , to some timescale of the carrier phase flow, τ_f .⁵⁷ Thus,

$$St = \frac{\tau_p}{\tau_f}. \quad (21)$$

The above dimensionless number characterizes the behavior of the particles dispersed in a fluid flow. Considering that a turbulent flow is characterized by a wide range of timescales corresponding to the spectrum of turbulent eddies, accordingly St can be calculated separately for eddies. In general, while $St \ll 1$ indicates that the particles act as flow tracers, $St > 1$ refers to ballistic behavior of the particles, i.e., they are not responsive to the velocity fluctuations of the fluid. The case of $St \approx 1$ is interesting as it indicates that the particles begin to respond to the turbulent eddies corresponding to which τ_f is considered in the above equation. In the present work, we calculate two different Stokes numbers: St_L based on the large-eddy timescale, τ_L , and St_η based on the Kolmogorov timescale, τ_η , where the timescales are evaluated as per the following expressions:

$$\tau_L = \frac{u_{rms}}{L}, \quad (22)$$

$$\tau_\eta = \left(\frac{v}{\epsilon} \right)^{0.5}, \quad (23)$$

where u_{rms} is the standard deviation of the gas velocity fluctuations, L is the large-eddy length scale that is taken as the jet half-width, $r_{1/2}$, at a particular axial location in an order of magnitude sense, v is the kinematic viscosity of the gas, and ϵ is the turbulent dissipation rate that is obtained using Eq. (7).

Frames (a)–(c) of Fig. 14 present the axial evolution of the particle Stokes number, St_L , for $\alpha = 0, 1$, and 1.5 , respectively. For each case, the results are shown for three particle size-classes, i.e., $25 \mu\text{m}$ – $50 \mu\text{m}$, $50 \mu\text{m}$ – $75 \mu\text{m}$, and $75 \mu\text{m}$ – $100 \mu\text{m}$. St_L of a given particle size-class is obtained by considering the mean size of that size-class. It can be observed that for a given spatial location in the jet, St_L is higher for larger particles (a higher size-class), which is expected and according to the definition of St_L as given in Eq. (21). Nevertheless, some interesting trends are observed, which are explained further in what follows:

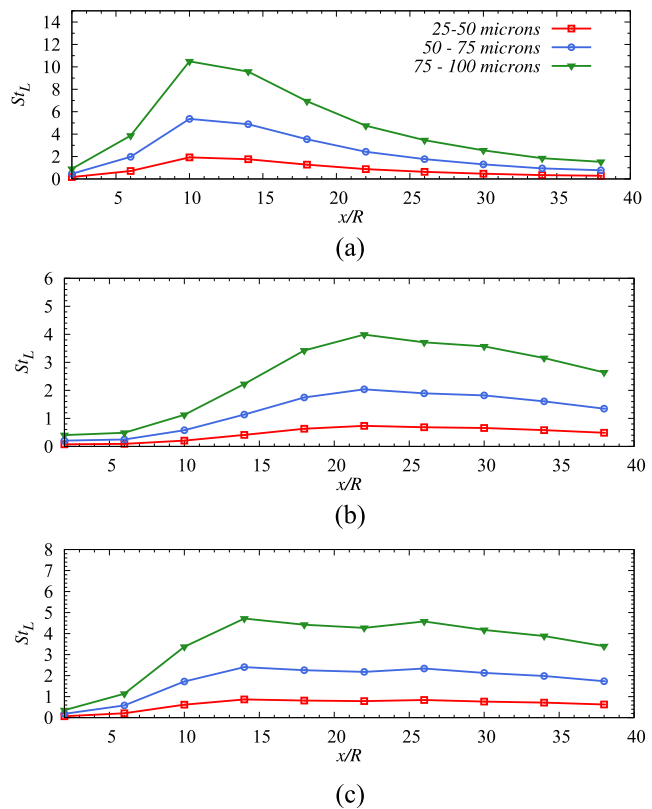


FIG. 14. Axial evolution of the particle Stokes number based on large-scale eddies, St_L , for particles of different size-classes and co-flow velocity ratios (a) $\alpha = 0$, (b) $\alpha = 1$, and (c) $\alpha = 1.5$.

- (i) It can be noted that for all particle size-classes, away from the nozzle exit, St_L first increases up to a peak value and then reduces though the rate of reduction varies according to the co-flow velocity ratio α . This trend of initial increase can be explained by considering the axial development of u_{rms} of the gas flow (refer to the u_{rms}/u_e vs x/R plot in Fig. 15). Beyond the jet exit, as the turbulence develops within the potential core region, the timescale of eddies reduces such that St_L increases along the axial direction, suggesting poor response of particles to turbulence as they move along the direction of the jet.

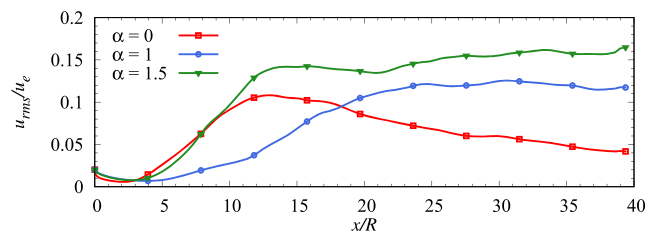


FIG. 15. Axial evolution of normalized u_{rms} along the jet centerline for indicated co-flow velocity ratios, α .

- (ii) In the absence of co-flow, for the case with $\alpha = 0$, the turbulent fluctuations reduce beyond the potential core. As the jet expands, the turbulent timescale increases; thus, St_L is smaller further downstream of the core region, as can be seen in frame (a) of Fig. 14. In contrast to the above, due to co-flow around the central jet, the turbulent intensity always increases along the jet flow direction, as can be seen from Fig. 6. However, as the half-width of the jet increases as well, the turbulent timescale does not vary much, and accordingly, St_L does not change much as one moves downstream.
- (iii) Comparing the magnitudes of St_L for different cases, it can be noted that due to co-flow around the central jet, the particle response to turbulence improves for all size-classes. In comparison with frame (a) of Fig. 14, the scale of St_L is smaller by a factor of $\sim 1/2$ in frames (b) and (c) of Fig. 14. This can be attributed to the generation of larger eddies for $\alpha = 1$ and 1.5 due to an additional shear layer that results due to the interaction between the central and the annular air flow. However, the values of St_L for a given particle size-class are nearly the same between the co-flow velocity ratios of $\alpha = 1$ and 1.5. Though the turbulent intensity profiles for these two cases are different, as can be seen in Fig. 15, the size of large-eddies (represented by $r_{1/2}$) does not change much. As a result, St_L for $\alpha = 1.5$ is only slightly larger than that for $\alpha = 1$.
- (iv) Although not presented here, the particle Stokes number based on the Kolmogorov scale, St_η , was also calculated as mentioned earlier. Though the trend of St_η was found to be similar to that of St_L , the magnitude of the former was much larger for all cases. Beyond the potential core of the jet and at the beginning of the decay zone, St_η was very high about 40–300 (larger for a higher particle size-class). Though its magnitude reduces thereafter, yet St_η was about 10–50 at the end of the simulation domain. The larger values of St_η indicate that in the present simulations, the behavior of dispersed particles is essentially ballistic in nature as far as their interaction with the smallest eddies of the flow is concerned. As a consequence, the particles tend to dissipate the energy at the small-scales of turbulence. In fact, this was further confirmed by comparing the axial evolution of the dissipation rate in the absence and presence of particles in turbulent jets, where it was observed that particles cause extra dissipation of energy especially in the early decay region where $St_\eta \gg 1$. This explains the earlier observation in Fig. 12, which indicates a small reduction in the mean gas velocity for the particle laden jet in comparison with the unladen case.

Finally, considering that the particle Stokes number was calculated in an order of magnitude sense, the ranges of St_η and St_L values as calculated above suggest that while the large particles that belong to 50 μm –75 μm and 75 μm –100 μm size-classes mostly do not respond to any turbulent fluctuations, the smaller particles that belong to the 25 μm –50 μm size-class, however, show a good to partial response to large-eddies but poor response to small-eddies.

D. Particle size-velocity correlation

Before discussing the particle dispersion in coaxial jets, it is important to present the evolution of particle size and particle velocity characteristics in particle-laden turbulent jets. In this section, we discuss the correlation between the instantaneous particle velocity and the particle size in coaxial jets. Figure 16 depicts a scatter plot between the particle size and the instantaneous particle velocity at some representative locations along the centerline of the jet for different co-flow velocity ratios, α .

At the near nozzle location, at $x/R = 10$, the local gas velocity is larger than the velocity of particles of all sizes. This means that all the particles are dragged by the gas flow. As smaller particles experience higher acceleration due to their lower inertia, they could quickly accelerate to attain the velocity of the gas. On the other hand, larger particles accelerate slowly, so their velocity is smaller. Accordingly, an inverse correlation exists, i.e., the larger the particle size, the lower its velocity. It can be observed that the results are similar for all α . However, the scatter of the data in the y -direction reduces for larger α , which can be explained below. As shown in Fig. 14, for $x/R = 10$, St_L of particles of three size-classes are large, $St_L > 1$, for $\alpha = 0$, indicating poor response to turbulent fluctuations suggesting a wider range of particle–gas slip-velocity. On the other hand, for a larger co-flow ratio, St_L reduces (for 25 μm –50 μm particles, $St_L < 1$), suggesting better response to turbulence and a narrower range of slip. Accordingly, the scatter of the data for a given particle size is higher for $\alpha = 0$, while it reduces considerably for $\alpha = 1$ and 1.5.

Further downstream of the jet at $x/R = 22$, similar results are obtained. However, the correlation can be observed to be weaker. This is because now the gas velocity has decayed, and the drag is smaller compared to that in the location at $x/R = 10$. As the particles are transported further downstream, the particle size–velocity correlation may change as shown in the plots for $x/R = 22$ and 34. For the case where co-flow is absent, $\alpha = 0$, the gas velocity decays rapidly such that larger particles now accelerate beyond the local gas velocity. Thus, the larger the particle size, the higher its velocity due to higher inertia, which results in a positive correlation. However, due to co-flow, this effect is further delayed as the local velocity of the gas is higher. Thus, a negative correlation is still observed for both $\alpha = 1$ and 1.5 even further downstream at $x/R = 22$ and 34. For both $x/R = 22$ and 34, the data scatter in the y -direction is reduced as the co-flow velocity ratio increases for the same reason as explained earlier. The particle size–velocity correlation obtained is approximated using a linear fit, and a regression coefficient, ζ , is calculated. Figure 17 shows the axial evolution of this regression coefficient, ζ , for the three co-flow velocity ratios. For $\alpha = 0$, the parameter, ζ , changes sign from a negative to a positive value around $x/R = 22$. However, for $\alpha = 1$, the sign of ζ changes further downstream at around $x/R = 32$, while it remains negative at all axial locations for $\alpha = 1.5$. These observations are in accordance with the aforementioned explanations.

E. Centerline average velocity of particles

While in Sec. III D, we discussed the instantaneous particle velocity and its correlation with the particle size, in this section, the average particle velocity in turbulent coaxial jets is considered.

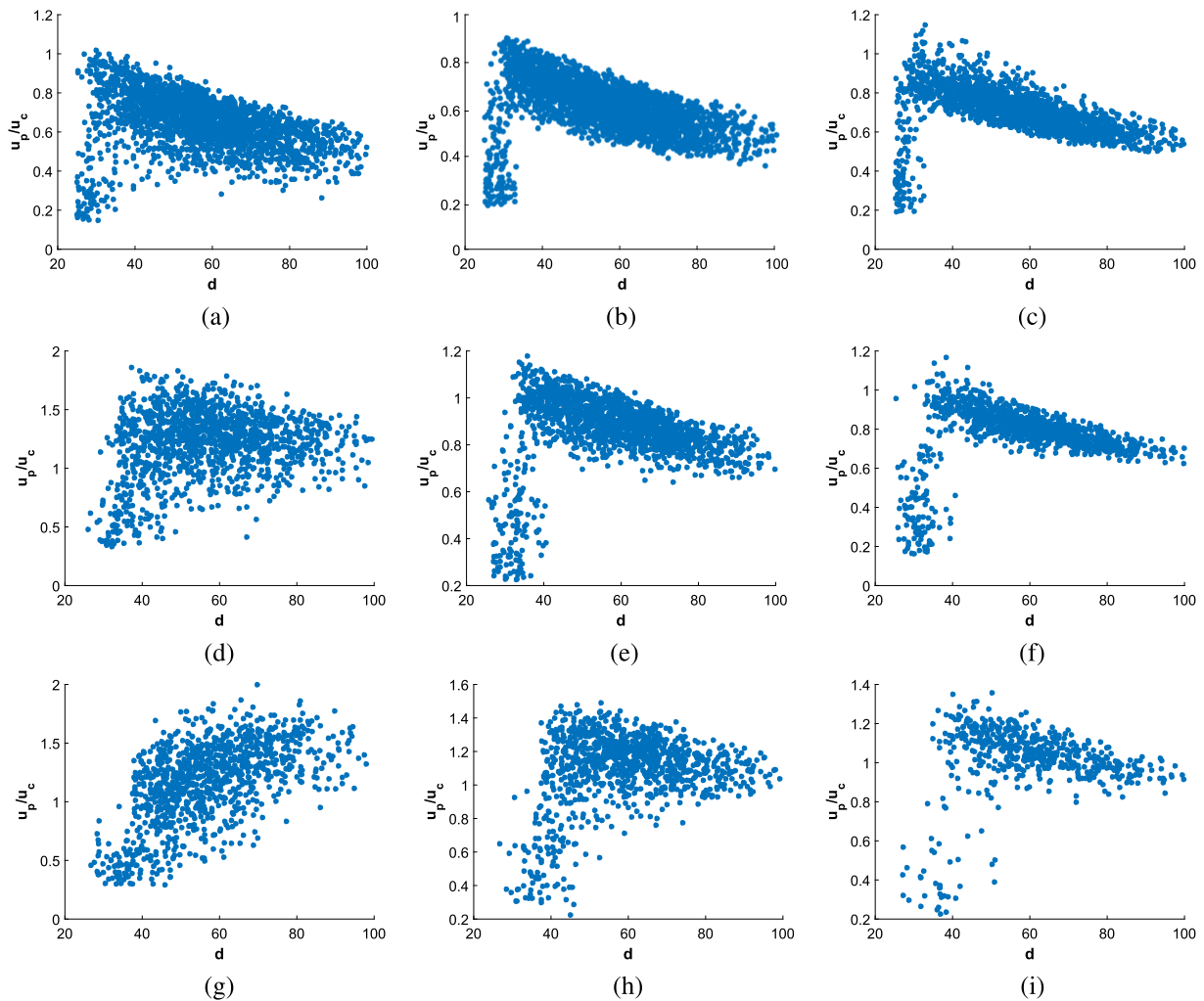


FIG. 16. Particle size–velocity correlation at different axial locations along the centerline of the jet for different co-flow velocity ratios, α . Each of the rows depicts a different axial location: frames (a)–(c) are for the location $x/R = 10$, frames (d)–(f) are for the location $x/R = 22$, and frames (g)–(i) are for the location $x/R = 34$. Each of the columns depicts a different co-flow velocity ratio, α : frames (a), (d), and (g) are for $\alpha = 0$, frames (b), (e), and (h) are for $\alpha = 1$, and frames (c), (f), and (i) are for $\alpha = 1.5$.

Figure 18 depicts the downstream evolution of the mean axial velocity of particles, $\langle u_p \rangle$, for different size-classes along the central axis of the domain. The mean velocity of the particle-laden gas phase, $\langle u \rangle$, is also plotted for the purpose of comparison. The local mean velocity of both the phases is normalized by the centerline gas velocity at the nozzle exit, u_e . The results are presented separately for different co-flow velocity ratios.

In general, two distinct behaviors of the average particle velocity can be noticed for all α depending on the location of the particles: whether within or outside the potential core region of the gas flow. Within the potential core zone, only a small reduction in the mean gas velocity occurs, while the velocity of the particles of all sizes increases monotonically from the nozzle exit (note that the particles are released at zero initial velocity). The plots for different particle size-classes are very close to each other for all α . Nevertheless,

close to the nozzle exit (for $3R < x < 5R$), the velocity is consistently higher for smaller particle size-classes, indicating faster acceleration of smaller particles (due to smaller relaxation time, τ_p , which is proportional to d_p^2). Beyond this and up to about $x/R \approx 10$, the trends for different particle sizes begin to deviate from each other, although not much difference in particle velocity is evident in this zone. In this region, as shown in Fig. 18, the mean gas velocity is always larger than that of the particles, which are dragged by the gas flow. This is in agreement with the particle size–velocity scatter plot at $x/R = 10$ in Fig. 16. Beyond the jet core region, the mean particle velocity varies according to the particle size as well as the co-flow velocity ratio, α , and this is discussed further in the following. It can be clearly observed that $50 \mu\text{m}$ – $75 \mu\text{m}$ and $75 \mu\text{m}$ – $100 \mu\text{m}$ particles tend to continue their initial trend and accelerate even beyond the mean gas velocity. This is attributed to their larger inertia. In

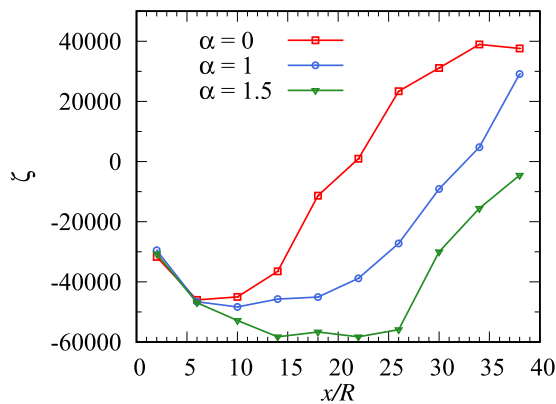


FIG. 17. Axial variation of the regression coefficient, ζ , for different co-flow ratios, $\alpha = 0, 1$, and 1.5 , along the centerline of the jet.

addition, the crossover points (where the mean particle velocity profiles meet the mean gas velocity profile) are shifted downstream as the co-flow velocity ratio α is made larger because the co-flow modifies the trend of the gas centerline velocity itself. However, once $\langle u_p \rangle$

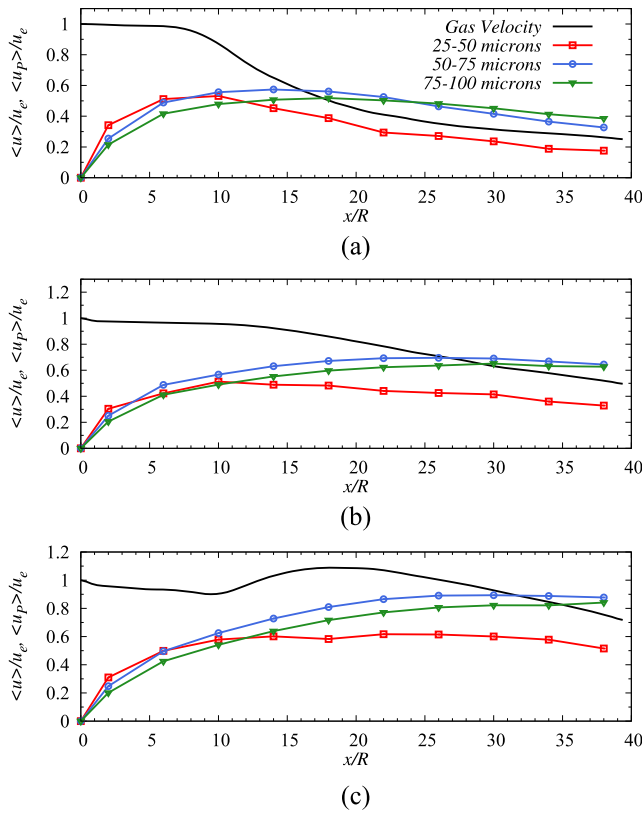


FIG. 18. Axial evolution of the centerline axial velocity of particles for different size-classes and co-flow velocity ratios (a) $\alpha = 0$, (b) $\alpha = 1$, and (c) $\alpha = 1.5$.

is larger than $\langle u \rangle$, the drag force opposes the particle motion such that their velocity reduces again. The positive correlation between particle size and velocity in Fig. 16 for $x/R = 34$ for $\alpha = 0$ supports this observation. This is evident clearly for the case of $\alpha = 0$ compared to the other two cases due to the limited extent of domain in the axial direction under consideration. In contrast to the large particles, the smaller 25 μm –50 μm particles are unable to match the gas velocity but tend to approach the latter as the particles move further downstream. Thus, the velocity of these particles reduces [frames (a) and (b) of Fig. 18] or remains nearly uniform [frame (c) of Fig. 18]. This means that unlike the larger particles, these particles are dragged by the gas flow through the entire domain under study. The above results show that in the present simulations, the smaller particles (25 μm –50 μm) “sense” the gas flow better than the larger particles, which are unable to adapt to the changes in gas velocity. This is in accordance with their corresponding St_L as explained earlier.

F. Effect of co-flow on particle dispersion

In this section, we discuss the dispersion of poly-dispersed particles that are injected into the turbulent jet. Specifically, the focus is on the influence of co-flow around the central jet. Figure 19 shows the axial evolution of the centerline average number density, $\langle N \rangle$, of the particles of different size-classes normalized by respective values at the nozzle exit, N_e . We note that the local number density of the particles (of a given size-class) was calculated by counting the number of particles in a predefined volume. The results are presented for different co-flow ratios, $\alpha = 0, 1$, and 1.5 , separately. It can be observed that for all cases, $\langle N \rangle / N_e$ reduces from the nozzle exit. This is attributed to the radial expansion of the jet as it develops downstream due to which the injected particles tend to disperse away from the jet axis. As a result, the number density of particles in all size-classes reduces downstream. Two important observations can be made now. First, one can notice the difference in the magnitude of $\langle N \rangle / N_e$ with the particle size. At any location, the number density of particles (relative to that at the nozzle exit) is higher for the 25 μm –50 μm range in comparison with 50 μm –75 μm and 75 μm –100 μm particles for which the plots almost overlap. Next, comparing frames (a)–(c) of Fig. 19, it was found that the plots for all three particle size-classes are shifted upward due to finite co-flow ($\alpha = 1$ and 1.5) in comparison with the case with no co-flow, $\alpha = 0$. However, the plots are shifted slightly downward for a higher co-flow velocity ratio, $\alpha = 1.5$, relative to that for $\alpha = 1$ [frames (b) and (c) of Fig. 19]. The above trends can be explained by considering the evolution of the particle Stokes number, St_L , in the jet as discussed earlier and also using radial variation of the particle number density, which is presented in the following.

Figure 20 presents, for different axial locations, the radial profiles of the normalized particle number density, $\langle N \rangle / \langle N \rangle_C$, where $\langle N \rangle_C$ is the average number density at the jet axis at the considered axial location, for different size-classes of particles. The results are presented for different co-flow ratios. For the near nozzle location, $x/R = 10$, the number density of 50 μm –75 μm and 75 μm –100 μm particles reduces significantly in the radial direction for all α . Due to their high Stokes number ($St_L > 1$ for all co-flow velocity ratios), these particles do not respond well to the gas flow.

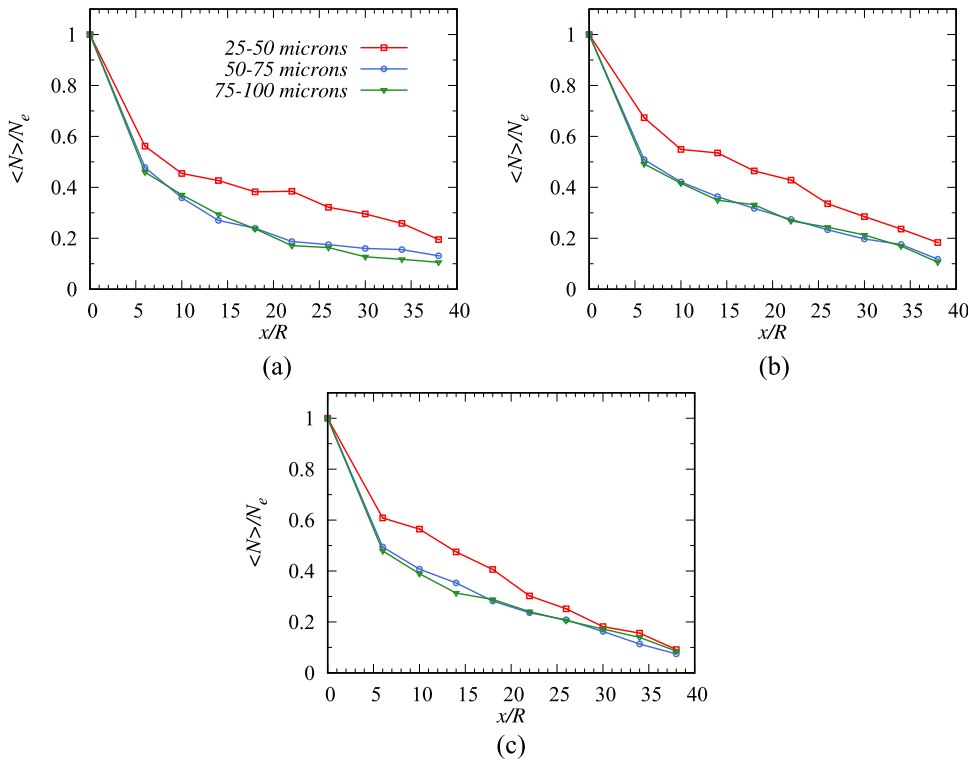


FIG. 19. Axial evolution of the normalized average particle number density, $\langle N \rangle / N_e$, for different size-classes and co-flow velocity ratios (a) $\alpha = 0$, (b) $\alpha = 1$, and (c) $\alpha = 1.5$.

Considering that the particles are injected with zero velocity, only the particles at the center are able to be drifted away as the centerline velocity is higher, while the off-centric particles experience reduced drag, so they are accelerated much slower. As a result, the particle number density reduces radially and more so significantly in the axial direction as observed in Fig. 19. However, the scenario is different for the smaller particles, with size $25\text{ }\mu\text{m}$ - $50\text{ }\mu\text{m}$. Due to their smaller St_L , in the absence of co-flow, $\alpha = 0$, and for $x/R = 10$, the $25\text{ }\mu\text{m}$ - $50\text{ }\mu\text{m}$ particles are able to disperse in the cross-stream direction since their St_L is about 1. Thus, they respond to large-eddy fluctuations that promote cross-stream particle dispersion such that their number density increases in the radial direction. However, as the co-flow velocity ratio is made larger, their St_L reduces even more ($St_L < 1$) so that they are dragged along the axial direction since the axial velocity is much stronger than the radial velocity. Further downstream of the jet, for instance, $x/R = 22$ and 34 , St_L of all particles reduces as explained in Sec. III C. Hence, even larger particles tend to respond to large-eddies; as a result, their number density increases in the radial direction. Hence, although the centerline number density reduces as the jet expands, the rate of reduction is smaller.

As mentioned earlier, the Stokes number St_L of particles varies according to the particle size, and in addition, St_L for the same particle changes as it is transported downstream of the nozzle. Accordingly, the dispersion characteristics vary within the turbulent jet. Hence, now we attempt to provide a general description of the particle dispersion characteristics. For this purpose, a radial dispersion parameter β is defined as follows:

$$\beta = \left(\frac{\langle N \rangle}{\langle N \rangle_C} \right)_{\max} - 1, \quad (24)$$

where $\left(\frac{\langle N \rangle}{\langle N \rangle_C} \right)_{\max}$ represents the maximum number density of particles of a given size-class at any axial location. The condition $\beta = 0$ refers to no radial dispersion and that all particles accumulate at the jet axis only, while a larger β means a higher number density of particles relative to that at the jet axis. Figure 21 plots the correlation between β and St_L for all simulation cases. It can be observed that the data points corresponding to larger values of β are clustered around $St_L \approx 1$, while β tends to be much smaller and close to zero for either $St_L \gg 1$ or $St_L \ll 1$. The above results further clarify the discussion of the results presented in the context of Figs. 18 and 19. Physically, this signifies that when the response time of particles is of the similar order as the timescale of large-eddies, the particles tend to respond to the gas phase turbulence in such a way that it leads to the so called preferential particle accumulation effect.^{7,65-68} As a consequence, the particles tend to accumulate in the peripheral region of the large-eddies and are thus transported away from the jet axis. However, this effect is subservient when the particle response time is either much larger or smaller relative to the turn-over time of large-eddies.

G. Axial evolution of AMD and SMD in coaxial jets

An evaluation of the characteristic particle size in the jet can exemplify the overall dispersion effect and is of practical interest. Hence, the average mean diameter (AMD) and Sauter mean

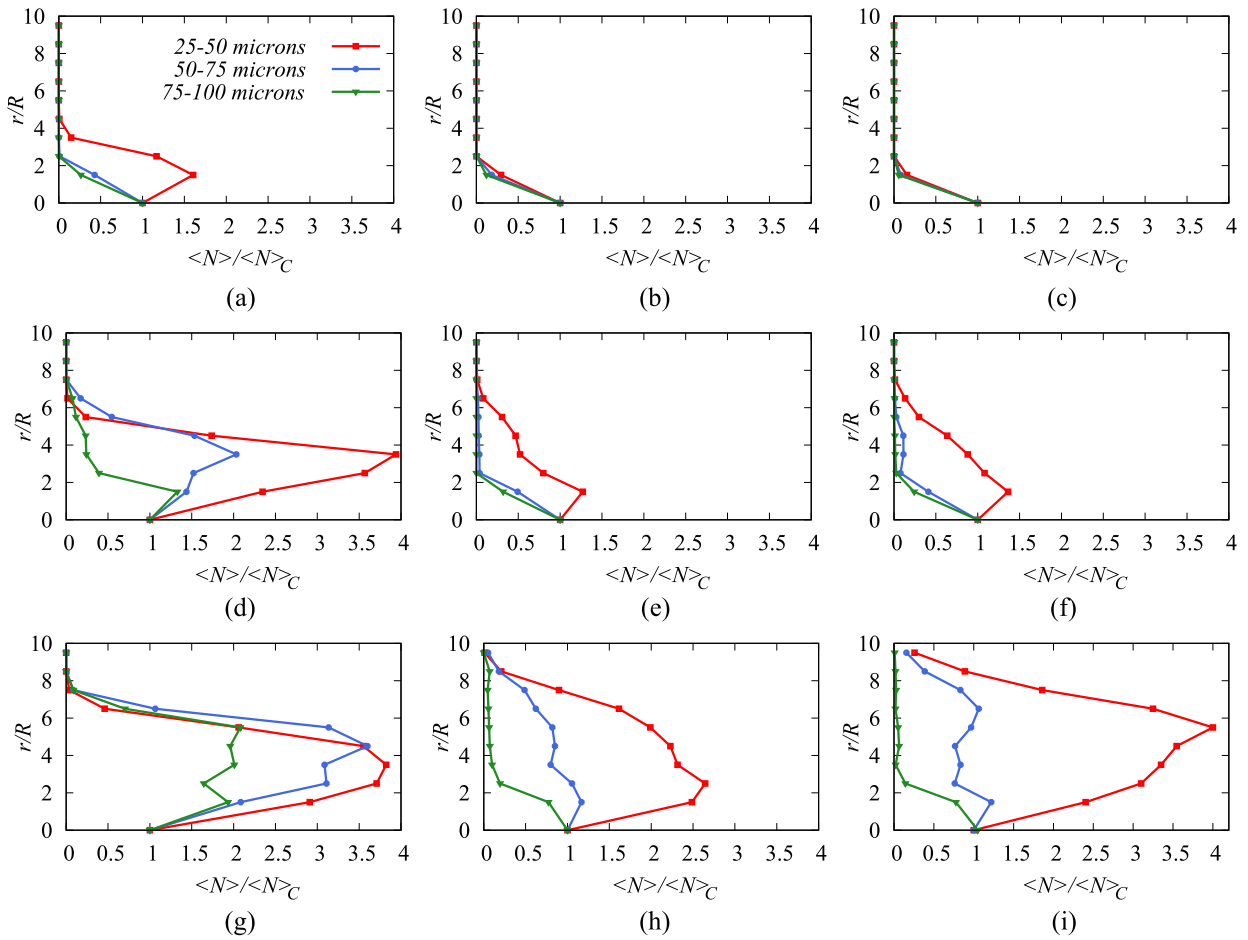


FIG. 20. Radial variation of the normalized average particle number density, $\langle N \rangle / \langle N \rangle_C$, at different axial locations and co-flow velocity ratios, α . Each of the rows depicts a different axial location: frames (a)–(c) are for the location $x/R = 10$, frames (d)–(f) are for the location $x/R = 22$, and frames (g)–(i) are for the location $x/R = 34$. Each of the columns depicts a different co-flow velocity ratio, α : frames (a), (d), and (g) are for $\alpha = 0$, frames (b), (e), and (h) are for $\alpha = 1$, and frames (c), (f), and (i) are for $\alpha = 1.5$.

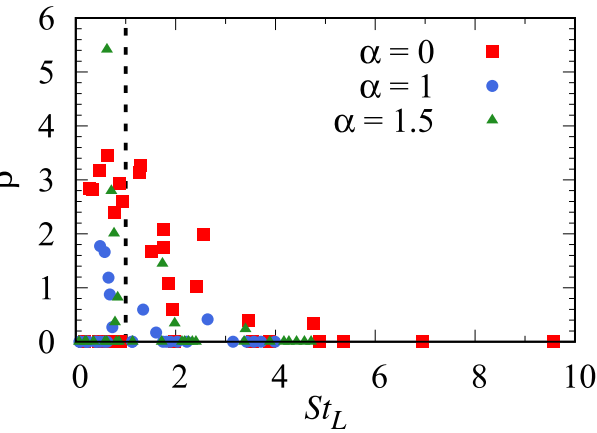


FIG. 21. Relationship between the radial dispersion parameter β and the Stokes number St_L , for different co-flow ratios, $\alpha = 0, 1$, and 1.5 .

diameter (SMD) of particle size are calculated for different axial locations considering all the particles across the jet at each axial location, as per the following equations:⁵⁷

$$AMD = \sum_{i=1}^M n_i d_{p_i} / \sum_{i=1}^M n_i, \quad (25)$$

$$SMD = \sqrt{\frac{\sum_{i=1}^M n_i d_{p_i}^3}{\sum_{i=1}^M n_i d_{p_i}^2}}, \quad (26)$$

where n_i is the number count of the i th particle with a diameter d_{p_i} and M is the total number of particles corresponding to the cross-sectional plane at a given axial location. We note that the AMD, as the name indicates, refers to the average size of the particles and is relevant in all dispersed multi-phase flow applications. In contrast, the SMD represents the size of a particle having the same volume to surface-area ratio of the entire set of particles. Thus, the SMD is useful in applications where the effective surface area of the particles

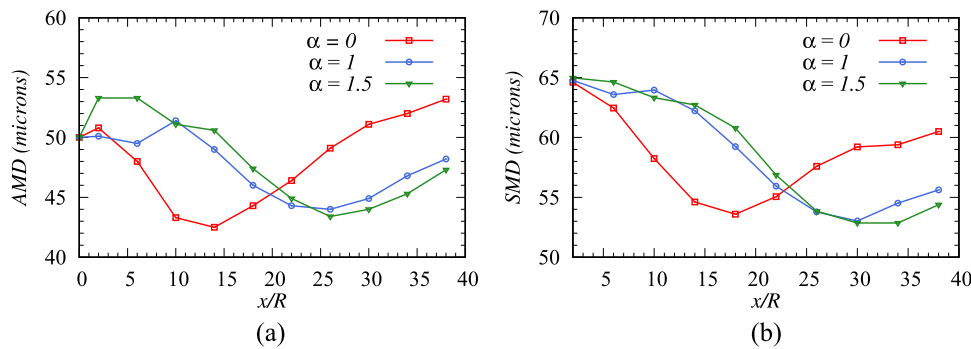


FIG. 22. Axial evolution of the (a) AMD and (b) SMD in turbulent jets with different co-flow ratios.

is important. For example, in combustion applications (e.g., droplets in sprays Ref. 69 or coal particles in coal-fired burners Ref. 3), high surface area of particles (or a lower SMD) is desirable to ensure efficient burning of the particles. In the present work, our interest is to examine the influence of the co-flow velocity ratio on the evolution of both the AMD and the SMD. Frames (a) and (b) of Fig. 22 present the axial evolution of the AMD and SMD, respectively, in the axial direction away from the nozzle exit. The observations made from these figures are explained in the following:

- (i) It is interesting to note that the characteristic particle sizes do not remain constant along the axis of the jet. For all velocity ratios, except for near the nozzle exit and beyond $x/R \approx 5-10$, both the AMD and the SMD first decrease and then increase. However, this trend appears to be shifted toward right for $\alpha = 1$ and 1.5 in comparison with $\alpha = 0$. An increasing trend is observed for $x/R < 5$ in the case of the AMD, which will be addressed separately.
- (ii) The above trend can be explained by considering both the axial and radial variations of the particle number density discussed earlier in the context of Figs. 19 and 20. Away from the nozzle exit, the reduction in the number density of larger particles is more than that for the smaller ($25 \mu\text{m}-50 \mu\text{m}$) particles. In addition, the particle number density of smaller particles increases radially. Thus, the size distribution is populated with smaller particles; as a result, the AMD and SMD reduce. However, further downstream of the jet, the large particles also tend to respond to large-eddies (their St_L being smaller) that makes them disperse radially. Thus, the probability of these particles increases; hence, the AMD and SMD increase again. For each profile, the presence of a minimum is evident that shifts toward right for higher α . Interestingly, for each case, the location of the minimum corresponds to a maximum in the St_L plot (see Fig. 14) that indicates poor response of the particles to turbulent flow of the continuous phase.
- (iii) It can be noted that for any axial location and for a given α , the value of the SMD is always larger than that of the AMD. This is because as per their definition [see Eq. (26)], the SMD is dictated by particles of larger size (due to higher power of the particle size). Nevertheless, except for the region very close to the nozzle exit, the overall trend of the AMD and SMD is similar.

- (iv) It can be observed that very close to the nozzle exit, $x/R < 5$, the AMD increases slightly, but the SMD does not vary much. This is possibly due to faster response of the small particles, which quickly get transported away from the nozzle leaving the larger particles behind. Thus, the AMD is larger; however, as the number density of larger particles does not change much, accordingly, the SMD is nearly the same.

IV. CONCLUSIONS

In the present study, LES was performed for coaxial jets with poly-disperse particles introduced in the central nozzle. The aim here is to study the evolution of particle dispersion in a turbulent jet; in particular, the focus is on the influence of different co-flow velocity ratios. The size of the injected particles followed the Rosin-Rammler distribution. Three different co-flow velocity ratios, $\alpha = 0$, 1, and 1.5, are considered in the present study. The results pertaining to the particle characteristics were presented in terms of three different size-classes: $25 \mu\text{m}-50 \mu\text{m}$, $50 \mu\text{m}-75 \mu\text{m}$, and $75 \mu\text{m}-100 \mu\text{m}$. The gas phase results matched well with the reference data from experiments.⁵ The centerline decay of the gas phase velocity, for the case with particles, was compared to the experimental data obtained by Budilarto.⁵ Few discrepancies were observed in this comparison, which are attributed to the difference in the velocity of injection of the particles at the inlet to the domain. In the present simulations, the particles are injected at zero velocity at the inlet to the domain and would absorb more momentum from the gas phase in order to accelerate, thereby reducing the momentum of the gas phase. However, further downstream, the results obtained showed a good match with the reference data. The following conclusions can be drawn from the present work:

- (i) The mean and second-order statistics obtained using the present LES show a good match with the reference data.⁵ The radial profiles of the axial velocity at different axial locations, the centerline axial velocity decay, and the radial profiles of the axial velocity fluctuation at different axial locations all of them showed a good match with reference experimental data.
- (ii) A comparison of mean velocities of both the particles and the gas flow indicated that the $25 \mu\text{m}-50 \mu\text{m}$ particles accelerate faster than the larger particles, nearly up to the potential core region beyond which the velocity of the small particles

reduces and is always smaller than the gas velocity, while the $50\text{ }\mu\text{m}$ – $75\text{ }\mu\text{m}$ and $75\text{ }\mu\text{m}$ – $100\text{ }\mu\text{m}$ particles continue to accelerate even beyond the gas velocity (at some crossover point), though their velocity reduces further downstream. The crossover point shifts farther in the axial direction as the co-flow ratio is made larger. The above behavior is according to the particle size–velocity correlation, which was found to be negative at the nozzle exit, but it tends to change sign and become positive downstream of the jet. Addition of the co-flow around the jet shifts the location where the sign change occurs downstream.

- (iii) The Stokes number of particles, St_L , based on large-scale turbulent eddies was evaluated for different size-classes. For each case, St_L was found to first increase within the potential core of the jet and then decrease as the jet develops further. The range of St_L reduced significantly due to co-flow, indicating improved particle response; however, a slight increase was noticed when α was increased from 1 to 1.5. All the particles show poor response to the smallest-eddies of turbulence.
- (iv) Along the jet centerline, the average number density, $\langle N \rangle$, of all particles reduces right from the nozzle exit. However, the local number density relative to that at the nozzle exit is always higher for $25\text{ }\mu\text{m}$ – $50\text{ }\mu\text{m}$ particles, while that for the larger size-classes nearly overlaps. In addition, the radial dispersion of the small particles is found to be much stronger compared to that of particles of larger size. In order to understand such size-based preferential segregation of particles in the jets and, in this context, the influence of co-flow around the central jet, the radial dispersion parameter, β , was defined. Here, $\beta = 0$ refers to no radial dispersion and that all particles accumulate at the jet axis only, while a larger β means a higher number density of particles relative to that at the jet axis. Interestingly, the correlation between β and St_L for all simulation cases indicated that larger values of β are clustered around $St_L \approx 1$. On the other hand, β tends to be much smaller and close to zero for either $St_L \gg 1$ or $St_L \ll 1$. This means that when particle response time is similar to large eddies, they respond to the gas velocity fluctuations in such a way that promotes cross-stream mixing. In such a case, the number density of particles increases radially. This is in contrast to the case when St_L is much larger or smaller than 1, as in this case the particles do not adapt to large-scale eddies. The number density of such particles reduces radially away from the jet axis such that these particles are depleted rapidly along the mean jet flow direction.
- (v) In order to signify the consequence of turbulent dispersion of particles on characteristic particle size, the *AMD* and *SMD* of particle size distribution are calculated, which first reduce axially and then increase. This is attributed to the axial evolution of St_L of particles as they are transported downstream. Closer to the nozzle exit, only smaller particles are dispersed in the jet so that the characteristic size of the particles reduces; however, further downstream of the jet, even larger particles are dispersed that results in a larger magnitude. In addition, the above trend shifts downstream for higher co-flow velocity ratios. The axial locations where *SMD* profiles attain a minimum are found to

be slightly downstream when compared to their corresponding locations where *AMD* profiles attain a minimum, for the corresponding co-flow velocity ratio.

The present computations of particle-laden coaxial turbulent jets demonstrate successful application of LES to study gas–solid flows, which find several engineering applications. In the present work, an attempt was made to furnish detailed parametric description of particle dispersion behavior. The findings from the present study provide some insights into the complex interaction of polydisperse particles in turbulent carrier flows.

ACKNOWLEDGMENTS

The authors gratefully acknowledge the computing resources provided on the VIRGO computing cluster by P. G. Senapathy Center for Computational Resources at Indian Institute of Technology (IIT) Madras. K.A. is grateful for the new-faculty initiation-grant, Grant No. MEE1617852NFIGKAME, awarded by IIT Madras.

DATA AVAILABILITY

The data that support the findings of this study are available from the corresponding author upon reasonable request.

REFERENCES

- ¹M. Tahmasebpoor, Y. Rahimvandi Noupoor, and P. Badamchizadeh, “Fluidity enhancement of hard-to-fluidize nanoparticles by mixing with hydrophilic nanosilica and fluid catalytic cracking particles: Experimental and theoretical study,” *Phys. Fluids* **31**, 073301 (2019).
- ²J. Wang, W. Huang, Y. Zhang, Y. Wu, H. Zhang, and G. Yue, “Particle trajectories in pipe flow considering particle–wall collisions,” *Phys. Fluids* **32**, 043307 (2020).
- ³X. Wen, H. Wang, Y. Luo, K. Luo, and J. Fan, “Evaluation of flamelet/progress variable model for laminar pulverized coal combustion,” *Phys. Fluids* **29**, 083607 (2017).
- ⁴S. Balachandar and J. K. Eaton, “Turbulent dispersed multiphase flow,” in *The Annual Review of Fluid Mechanics* (Annual Reviews, 2010).
- ⁵S. Budilaro, “An experimental study on effects of fluid aerodynamics and particle size distributions in particle laden jet flows.” Ph.D. thesis, Purdue University, 2003.
- ⁶S. Sahu, Y. Hardalupas, and A. M. K. P. Taylor, “Droplet-turbulence interaction in a confined polydispersed spray: Effect of droplet size and flow length scales on spatial droplet-gas velocity correlations,” *J. Fluid Mech.* **741**, 98–138 (2014).
- ⁷M. Manish and S. Sahu, “Analysis of droplet clustering in air-assist sprays using Voronoi tessellations,” *Phys. Fluids* **30**, 123305 (2018).
- ⁸F. H. Champagne and I. J. Wygnanski, “An experimental investigation of coaxial turbulent jets,” *Int. J. Heat Mass Transfer* **14**, 1445–1464 (1971).
- ⁹N. A. Chigier and J. M. Beér, “The flow region near the nozzle in double concentric jets,” *J. Basic Eng.* **86**, 797–804 (1964).
- ¹⁰R. Sadr and J. C. Klewicki, “Flow field characteristics in the near field region of particle-laden coaxial jets,” *Exp. Fluids* **39**, 885–894 (2005).
- ¹¹Y. Tsuji, Y. Morikawa, T. Tanaka, K. Karimine, and S. Nishida, “Measurement of an axisymmetric jet laden with coarse particles,” *Int. J. Multiphase Flow* **14**, 565–574 (1988).
- ¹²Y. Hardalupas, A. M. K. P. Taylor, J. H. Whitelaw, and F. J. Weinberg, “Velocity and particle-flux characteristics of turbulent particle-laden jets,” *Proc. R. Soc. London, Ser. A* **426**, 31–78 (1989).
- ¹³H. J. Sheen, B. H. Jou, and Y. T. Lee, “Effect of particle size on a two-phase turbulent jet,” *Exp. Therm. Fluid Sci.* **8**, 315–327 (1994).
- ¹⁴A. A. Mostafa, H. C. Mongia, V. G. McDonell, and G. S. Samuelsen, “An experimental and numerical study of particle-laden coaxial jet flows,” *Int. J. Heat Fluid Flow* **11**, 90–97 (1990).

- ¹⁵J. Fan, H. Zhao, and K. Cen, "Particle concentration and size measurements in two-phase turbulent coaxial jets," *Chem. Eng. Commun.* **156**, 115–119 (1996).
- ¹⁶X. Jiang, G. A. Siamas, K. Jagus, and T. G. Karayannidis, "Physical modelling and advanced simulations of gas-liquid two-phase jet flows in atomization and sprays," *Prog. Energy Combust. Sci.* **36**, 131–167 (2010).
- ¹⁷S. Subramaniam, "Lagrangian-Eulerian methods for multiphase flows," *Prog. Energy Combust. Sci.* **39**, 215–245 (2013).
- ¹⁸X. Wang, X. Zheng, and P. Wang, "Direct numerical simulation of particle-laden plane turbulent wall jet and the influence of Stokes number," *Int. J. Multiphase Flow* **92**, 82–92 (2017).
- ¹⁹L.-P. Wang, B. Rosa, H. Gao, G. He, and G. Jin, "Turbulent collision of inertial particles: Point-particle based, hybrid simulations and beyond," *Int. J. Multiphase Flow* **35**, 854–867 (2009), special issue: Point-particle model for disperse turbulent flows.
- ²⁰M. Bernardini, S. Pirozzoli, and P. Orlandi, "The effect of large-scale turbulent structures on particle dispersion in wall-bounded flows," *Int. J. Multiphase Flow* **51**, 55–64 (2013).
- ²¹K. Luo, N. Gui, J. Fan, and K. Cen, "Direct numerical simulation of a two-phase three-dimensional planar jet," *Int. J. Heat Mass Transfer* **64**, 155–161 (2013).
- ²²S. Tenneti and S. Subramaniam, "Particle-resolved direct numerical simulation for gas-solid flow model development," *Annu. Rev. Fluid Mech.* **46**, 199–230 (2014).
- ²³Q. Dai, T. Jin, K. Luo, and J. Fan, "Direct numerical simulation of a three-dimensional spatially evolving compressible mixing layer laden with particles. I. Turbulent structures and asymmetric properties," *Phys. Fluids* **31**, 083302 (2019).
- ²⁴Q. Dai, T. Jin, K. Luo, W. Xiao, and J. Fan, "Direct numerical simulation of a three-dimensional spatially evolving compressible mixing layer laden with particles. II. Turbulence anisotropy and growth rate," *Phys. Fluids* **31**, 083303 (2019).
- ²⁵F. Zhao, W. K. George, and B. G. M. Van Wachem, "Four-way coupled simulations of small particles in turbulent channel flow: The effects of particle shape and Stokes number," *Phys. Fluids* **27**, 083301 (2015).
- ²⁶J. Pedel, J. N. Thorneock, S. T. Smith, and P. J. Smith, "Large eddy simulation of polydisperse particles in turbulent coaxial jets using the direct quadrature method of moments," *Int. J. Multiphase Flow* **63**, 23–28 (2014).
- ²⁷M. Alletto and M. Breuer, "One-way, two-way and four-way coupled LES predictions of a particle-laden turbulent flow at high mass loading downstream of a confined bluff body," *Int. J. Multiphase Flow* **45**, 70–90 (2012).
- ²⁸M. Alletto and M. Breuer, "Prediction of turbulent particle-laden flow in horizontal smooth and rough pipes inducing secondary flow," *Int. J. Multiphase Flow* **55**, 80–98 (2013).
- ²⁹A. S. Berrouk, D. E. Stock, D. Laurence, and J. J. Riley, "Heavy particle dispersion from a point source in turbulent pipe flow," *Int. J. Multiphase Flow* **34**, 916–923 (2008).
- ³⁰G. Jin, G.-W. He, and L.-P. Wang, "Large-eddy simulation of turbulent collision of heavy particles in isotropic turbulence," *Phys. Fluids* **22**, 055106 (2010).
- ³¹Q. Wang and K. D. Squires, "Large eddy simulation of particle-laden turbulent channel flow," *Phys. Fluids* **8**, 1207–1223 (1996).
- ³²K. Kannaiyan and R. Sadr, "Numerical simulation of particle-laden coaxial turbulent jets," *Int. J. Comput. Methods Eng. Sci. Mech.* **14**, 61–73 (2013).
- ³³Y. Xu and S. Subramaniam, "Consistent modeling of interphase turbulent kinetic energy transfer in particle-laden turbulent flows," *Phys. Fluids* **19**, 085101 (2007).
- ³⁴A. A. Mofakham and G. Ahmadi, "Particles dispersion and deposition in inhomogeneous turbulent flows using continuous random walk models," *Phys. Fluids* **31**, 083301 (2019).
- ³⁵C. Jin, I. Potts, and M. W. Reeks, "A simple stochastic quadrant model for the transport and deposition of particles in turbulent boundary layers," *Phys. Fluids* **27**, 053305 (2015).
- ³⁶M. Sommerfeld, A. Ando, and D. Wennerberg, "Swirling, particle-laden flows through a pipe expansion," *J. Fluids Eng.* **114**, 648–656 (1992).
- ³⁷S. V. Apte, K. Mahesh, P. Moin, and J. C. Oefelein, "Large-eddy simulation of swirling particle-laden flows in a coaxial-jet combustor," *Int. J. Multiphase Flow* **29**, 1311–1331 (2003).
- ³⁸R. Kurose, H. Watanabe, and H. Makino, "Numerical simulations of pulverized coal combustion," *KONA Powder Part. J.* **27**, 144–156 (2009).
- ³⁹T. N. Aziz, J. P. Raiford, and A. A. Khan, "Numerical simulation of turbulent jets," *Eng. Appl. Comput. Fluid Mech.* **2**, 234–243 (2008).
- ⁴⁰M. Olsson and L. Fuchs, "Large eddy simulation of the proximal region of a spatially developing circular jet," *Phys. Fluids* **8**, 2125–2137 (1996).
- ⁴¹K. Askselvoll and P. Moin, "Large-eddy simulation of turbulent confined coannular jets," *J. Fluid Mech.* **315**, 387–411 (1996).
- ⁴²I. Tkatchenko, N. Kornev, S. Jahnke, G. Steffen, and E. Hassel, "Performances of LES and RANS models for simulation of complex flows in a coaxial jet mixer," *Flow, Turbul. Combust.* **78**, 111–127 (2006).
- ⁴³A. W. Abboud and S. T. Smith, "Large eddy simulation of a coaxial jet with a synthetic turbulent inlet," *Int. J. Heat Fluid Flow* **50**, 240–253 (2014).
- ⁴⁴M. Klein, A. Sadiki, and J. Janicka, "A digital filter based generation of inflow data for spatially developing direct numerical or large eddy simulations," *J. Comput. Phys.* **186**, 652–665 (2003).
- ⁴⁵N. Jarrin, S. Benhamadouche, D. Laurence, and R. Prosser, "A synthetic-eddy-method for generating inflow conditions for large-eddy simulations," *Int. J. Heat Fluid Flow* **27**, 585–593 (2006).
- ⁴⁶H. G. Weller, G. Tabor, H. Jasak, and C. Fureby, "A tensorial approach to computational continuum mechanics using object-oriented techniques," *Comput. Phys.* **12**, 620 (1998).
- ⁴⁷OpenCFD, OpenFOAM—The Open Source CFD Toolbox—User's Guide, OpenCFD Ltd., 2019.
- ⁴⁸W.-W. Kim and S. Menon, "A new dynamic one-equation subgrid-scale model for large eddy simulations," in 33rd Aerospace Sciences Meeting and Exhibit, 1995.
- ⁴⁹M. V. Tabib and P. Schwarz, "Quantifying sub-grid scale (SGS) turbulent dispersion force and its effect using one-equation SGS large eddy simulation (LES) model in a gas-liquid and a liquid-liquid system," *Chem. Eng. Sci.* **66**, 3071–3086 (2011).
- ⁵⁰N. Bharadwaj, C. J. Rutland, and S. Chang, "Large eddy simulation modelling of spray-induced turbulence effects," *Int. J. Engine Res.* **10**, 97–119 (2009).
- ⁵¹N. Bharadwaj and C. J. Rutland, "A large-eddy simulation study of sub-grid two-phase interaction in particle-laden flows and diesel engine sprays," *Atomization Sprays* **20**, 673–695 (2010).
- ⁵²M. Bini and W. P. Jones, "Large-eddy simulation of particle-laden turbulent flows," *J. Fluid Mech.* **614**, 207–252 (2008).
- ⁵³V. Armenio, U. Piomelli, and V. Fiorotto, "Effect of the subgrid scales on particle motion," *Phys. Fluids* **11**, 3030–3042 (1999).
- ⁵⁴A. Putnam, "Integrable form of droplet drag coefficient," *ARS J.* **31**, 1467–1468 (1961).
- ⁵⁵F. Toschi and E. Bodenschatz, "Lagrangian properties of particles in turbulence," *Annu. Rev. Fluid Mech.* **41**, 375–404 (2009).
- ⁵⁶S. Olivieri, F. Picano, G. Sardina, D. Iudicone, and L. Brandt, "The effect of the Basset history force on particle clustering in homogeneous and isotropic turbulence," *Phys. Fluids* **26**, 041704 (2014).
- ⁵⁷C. T. Crowe, J. D. Schwarzkopf, M. Sommerfeld, and Y. Tsuji, *Multiphase Flows with Droplets and Particles* (CRC Press, 2011).
- ⁵⁸R. A. Mugele and H. D. Evans, "Droplet size distribution in sprays," *Ind. Eng. Chem.* **43**, 1317–1324 (1951).
- ⁵⁹K. B. Wilbur and H. W. Kenneth, "Derivation of the Weibull distribution based on physical principles and its connection to the Rosin-Rammler and lognormal distributions," *J. Appl. Phys.* **78**, 2758–2763 (1995).
- ⁶⁰A. Dejoan and M. A. Leschziner, "Large eddy simulation of a plane turbulent wall jet," *Phys. Fluids* **17**, 025102 (2005).
- ⁶¹I. Orlanski, "A simple boundary condition for unbounded hyperbolic flows," *J. Comput. Phys.* **21**, 251–269 (1976).
- ⁶²G. R. Tabor and M. H. Baba-Ahmadi, "Inlet conditions for large eddy simulation: A review," *Comput. Fluids* **39**, 553–567 (2010).
- ⁶³P. Sagaut, S. Deck, and M. Terracol, *Multiscale and Multiresolution Approaches in Turbulence*, 2nd ed. (Imperial College Press, 2013).

- ⁶⁴N. S. Dhamankar, G. A. Blaisdell, and A. S. Lyrintzis, "Overview of turbulent inflow boundary conditions for large-eddy simulations," *AIAA J.* **56**, 1317–1334 (2018).
- ⁶⁵E. K. Longmire and J. K. Eaton, "Structure of a particle-laden round jet," *J. Fluid Mech.* **236**, 217–257 (1992).
- ⁶⁶A. Ferrante and S. Elghobashi, "On the physical mechanisms of two-way coupling in particle-laden isotropic turbulence," *Phys. Fluids* **15**, 315–319 (2003).
- ⁶⁷S. Sahu, Y. Hardalupas, and A. M. K. P. Taylor, "Droplet-turbulence interaction in a confined polydispersed spray: Effect of turbulence on droplet dispersion," *J. Fluid Mech.* **794**, 267–309 (2016).
- ⁶⁸M. Manish and S. Sahu, "Droplet clustering and local spray unsteadiness in air-assisted sprays," *Exp. Therm. Fluid Sci.* **100**, 89–103 (2019).
- ⁶⁹A. Kumar and S. Sahu, "Liquid jet disintegration memory effect on downstream spray fluctuations in a coaxial twin-fluid injector," *Phys. Fluids* **32**, 073302 (2020).